Aryl hydrocarbon receptor restricts axon regeneration of DRG neurons in response to injury

Dalia Halawani [1,*], Yiqun Wang [1,2,*], Molly Estill [1], Arthur Sefiani [3], Aarthi Ramakrishnan [1], Jiaxi Li [1,5], Haofei Ni [1,4], Daniel Halperin [1], Li Shen [1], Cédric G. Geoffroy [3], Roland H. Friedel [1,5], Hongyan Zou [1,5,#]

[1] Nash Family Department of Neuroscience, Friedman Brain Institute, Icahn School of Medicine at Mount Sinai, New York, USA

[2] Sport Medicine Center, Honghui Hospital, Xi'an Jiaotong University, Xi'an, China

[3] Department of Neuroscience and Experimental Therapeutics, College of Medicine, Texas A&M University, USA

[4] Division of Spine, Department of Orthopedics, Tongji Hospital, Tongji University School of Medicine, Shanghai, China

[5] Department of Neurosurgery, Icahn School of Medicine at Mount Sinai, New York, USA

*Equal Contribution

Corresponding author: hongyan.zou@mssm.edu

Abstract

Injured neurons sense environmental cues to balance neural protection and axon regeneration, but the mechanisms are unclear. Here, we unveil aryl hydrocarbon receptor (AhR), a ligand-activated bHLH-PAS transcription factor, as a molecular sensor and key regulator of acute stress response at the expense of axon regeneration. We demonstrate responsiveness of DRG sensory neurons to AhR signaling, which functions to inhibit axon regeneration. Conditional *Ahr* deletion in neurons accelerates axon regeneration after sciatic nerve injury. *Ahr* deletion partially mimics the conditioning lesion in priming DRG to initiate axonogenesis gene programs; upon peripheral axotomy, *Ahr* ablation suppresses inflammation and stress signaling while augmenting pro-growth pathways. Moreover, comparative transcriptomics revealed signaling interactions between AhR and HIF-1α, two structurally related bHLH-PAS α units that share the dimerization partner Arnt/HIF-1β. Functional assays showed that the growth advantage of AhR-deficient DRG neurons requires HIF-1α; but in the absence of Arnt, DRG neurons can still mount a regenerative response. We further unveil a link between bHLH-PAS transcription factors and DNA hydroxymethylation in response to peripheral axotomy, while RNA-seq of DRG neurons and neuronal single cell RNA-seq analysis revealed a link of AhR regulon to RNA regulation and integrated stress response (ISR). Altogether, AhR activation favors stress coping and inflammation at the expense of axon regeneration; targeting AhR has the potential to enhance nerve repair.

Key words:

Aryl hydrocarbon receptor (AhR), Axon regeneration, Conditioning lesion of DRG, Spinal cord injury, Hypoxia-inducible factor (HIF), Arnt, DNA hydroxymethylation, Integrated stress response (ISR).

Introduction

Injured neurons experience alteration of their environment due to inflammation, tissue damage, change in microbial populations or oxygen tension. Safeguard mechanisms have evolved to allow injured neurons to sense external cues to cope with stress, adjust metabolism or synaptic transmission, and launch regenerative gene programs. Timely execution of these tasks requires precise transcriptional rewiring, but the underlying mechanisms remain opaque.

The basic helix-loop-helix/PER-ARNT-SIM (bHLH-PAS) transcription factors (TFs) have evolved as molecular sensors of physiological and environmental cues, e.g., circadian activity, hypoxia, and xenobiotic exposure [1,2]. A recent study from our laboratory has uncovered a role of Bmal1, a core circadian regulator, in gating regenerative responses of dorsal root ganglia (DRG) sensory neurons after peripheral axotomy [3]. Activation of hypoxia-inducible factor (HIF)-1α through intermittent hypoxia can promote axon regeneration of DRG neurons [4]. Aryl hydrocarbon receptor (AhR) and HIF-1α are two structurally related α units of bHLH-PAS TFs that share the dimerization partner aryl hydrocarbon receptor translocator (Arnt, a.k.a. HIF-1β). The function of AhR or Arnt in axonal injury and their signaling relationship with HIF or Bmal1 have not been explored.

Initially characterized as a molecular sensor of environmental toxins such as dioxin, AhR is the only ligand-activated bHLH-PAS TF that can bind to a broad spectrum of dietary, microbial, and metabolic compounds [5]. Ligand binding triggers nuclear translocation of AhR and subsequent dimerization with Arnt to initiate context-specific transcriptional responses via AhR response element (AHRE; also termed xenobiotic response element (XRE) or dioxin response element (DRE)) [6]. One hallmark of canonical AhR signaling is the AHRE-driven induction of cytochrome P450 enzymes (Cyp1a1, Cyp1a2, and Cyp1b) for detoxification, as well as NRF2-dependent anti-oxidation genes [7,8]. AhR signaling is tightly controlled, as Cyp1 enzymes also metabolize AhR ligands, thus constituting an

inhibitory feedback loop to terminate AhR activity [9]. AhR activation also induces its own repressor, the AhR repressor (AhRR) [10], which not only dimerizes with Arnt and competes for AHRE occupancy, but also inhibits AHRE-driven genes via chromatin reconfiguration [11]. The multiple feedback inhibition mechanisms underscores the physiological importance of avoiding toxicity from prolonged AhR signaling [6].

Competition with HIF-1α for Arnt may also restrict AhR activity [12,13], but the antagonistic competition between AhR and HIF-1α is highly context-dependent [14-16], and in some scenarios they may act cooperatively [16] or even synergistically for gene regulation [17] . Recent study from the Quintana laboratory also revealed a temporally controlled access to Arnt, with HIF-1α acting first and then AhR taking over, adding further complexity of the crosstalk [16].

Previous studies on AhR have largely focused on toxicology, barrier tissue integrity, and immunology; less is understood of the function of AhR in axon regeneration and interplay with HIF-1α/Arnt. Here, we took advantage of a unique feature of DRG neurons wherein peripheral but not central axotomy triggers robust axon regeneration [18,19]. We demonstrated responsiveness of DRG neurons to ligand-mediated AhR signaling. Functional assays with AhR agonists/antagonists and conditional gene deletion revealed an inhibitory role of AhR for axon regeneration. We further defined the AhR injury regulon and signaling relationships with HIF-1α and Arnt in balancing stress coping and axon regeneration. These new understandings may advance neural repair strategies.

Results

DRG neurons display responsiveness to ligand-mediated AhR signaling

To understand transcriptional mechanisms in response to axotomy, we analyzed a set of early response TFs that we had identified in axotomized DRG at 12 or 24 hr after peripheral lesion (PL, regenerative) as compared to central lesion (CL, non-regenerative) [20]. These included well-known regeneration-associated TFs such as ATF3 [21], Sox11 [22], Jun [23], Smad1 [20,24], ATF4 [25], early response genes EGR1 and CREM, as well as AhR. STRING analysis [26] revealed an interconnected network of these TFs but no known functional connection with AhR (**Fig. 1a**). This also applied to a larger set of 39 TFs predicted to be linked to axon regeneration [27], showing interconnection between Smad, Fos, Stat, and Jun, but no known connection with AhR (**Fig. S1a**).

As AhR is the only ligand-activated bHLH-PAS TF, we first assessed responsiveness of adult DRG neurons to AhR agonist ITE (an indole-derived dietary compound and a physiological ligand of AhR with many disease modulatory roles [28-30]) and a ligand-selective AhR antagonist CH-223191 (CH) [31] (**Fig. 1b)**. Immunocytochemistry (ICC) revealed rapid nuclear translocation of AhR by ITE, but cytoplasmic retention by CH (**Fig. 1b**). Notably, primary DRG neurons maintained in serum-free defined media displayed baseline AhR nuclear immunosignals even after 4 days in vitro, signifying the presence of endogenous AhR ligands.

As a direct readout of AhR transcriptional activity, we next examined the expression of *Cyp1a1* and *Cyp1b1,* two canonical AhR target genes in the detoxification pathway, as well as *Ahrr*, a bHLH-PAS TF acting in the negative feedback loop (**Fig. 1c**). qRT-PCR demonstrated the expected induction or suppression of these AhR target genes by agonists or antagonist, respectively (**Fig. 1d**). In congruence, in vivo intraperitoneal injection of ITE for 3 days also induced *Cyp1a1, Cyp1b1* expression, and a trend for upregulation of *Ahrr* in DRG, shown by qRT-PCR or Western blots (WB) (**Fig. 1e, f**). WB

also revealed an electrophoretic mobility shift of AhR, reflecting post-translational modifications upon ligand stimulation.

Surveying a human tissue gene expression atlas revealed a higher expression of *AHR* in peripheral nerve than in brain or other non-neural tissues for both female and male, hinting at a unique role of AhR for nerve physiology (**Fig. S1b**). Analysis of single cell RNA-sequencing (scRNA-seq) data of mouse nervous system [32] further revealed transcripts of *Ahr*, *Hif1a*, and *Arnt* in a variety of CNS and PNS neurons, including DRG neurons, with a particularly high expression of *Cyp1b1* in peptidergic DRG neuron subtypes (**Fig. S1c**). Together these initial data illustrate responsiveness of DRG neurons to ligand-mediated AhR signaling.

AhR antagonist promotes neurite outgrowth and neuronal *Ahr* ablation enhances axonal regeneration

To probe the function of AhR, we first conducted *Ahr* siRNA knockdown in adult DRG neurons, which led to longer neurites (**Fig. 1g**). We next tested AhR agonist or antagonist on induced neurons derived from human embryonic stem cells (**Fig. 1h**). Application of AhR agonist Norisoboldine led to shorter neurites, whereas AhR antagonist CH 223191 resulted in longer neurites (**Fig. 1h**). These results were confirmed in a larger screen in a dose-dependent manner (**Fig. S2a**).

Similar axon growth promoting or inhibiting effects of AhR antagonist or agonist were also obtained with primary adult DRG neurons (**Fig. S2b**). Notably, the growth inhibitory effect of AhR agonist was only observed in cultured DRG neurons with continuous exposure to ITE, but not in those with transient in vivo exposure to ITE (**Fig. S2c**), in line with transient nature of AhR signaling due to multiple negative feedback mechanisms [6]. In addition, AhR antagonist StemRegenin1 (SR1) was independently identified in an unbiased high-throughput screen for compounds that enhance neurite

outgrowth of adult cortical neurons [33], leading to 28% increase in neurite length and 58% increase in neurite initiation relative to vehicle (**Fig. S2d**).

To corroborate our findings, we generated *Ahr* conditional knockout (cKO) mice by breeding *Ahr*$^{fl/fl}$ with *Nestin*^{Cre} allele [34,35] (**Fig. 2a**). WB confirmed marked reduction of AhR in both brain and DRG tissues from cKO mice (**Fig. 2b**). PL-triggered AhR induction was also markedly attenuated in *Ahr*^{cKO} DRG, but still slightly higher than in naive DRG, indicating non-neural source of AhR (**Fig. 2c**).

While constitutive *Ahr* deletion results in demyelinating disease and inflammation [36,37], *Ahr* cKO $^{Nes\text{-}Cre}$ mice appeared healthy and fertile with no overt motosensory deficits (**Fig. S3a**). We next performed sciatic nerve crush injury and examined sensory axon regeneration by conducting IF staining for SCG10, a marker that specifically labels regenerating but not uninjured sensory axons [38] (**Fig. 2d, e**). Consistent with the results from AhR antagonists, *Ahr* conditional deletion also promoted axon regeneration, with more and longer SCG10^{+} axons extending beyond the crush site at 2-day post injury (dpi), as measured by regenerative index and maximal axonal length (1.44 mm vs. 1.06 mm, a 36% increase) (**Fig. 2e**). Motosensory behavioral assays also showed accelerated functional recovery of *Ahr* cKO mice, with improved hindlimb toe spreading and better sciatic functional index (SFI) from 9 dpi through 21 dpi, and hindpaw skin re-innervation was also improved, with more abundant PGP9.5^{+} axons at 21 dpi (**Fig. S3b-d)**.

For further confirmation, we next generated *Ahr* cKO mice for time-controlled neuronal deletion of *Ahr* by crossing *Ahr*$^{fl/fl}$ to Thy1-Cre^{ERT2}/-EYFP (SLICK-H) mice [39,40] (**Fig. 2f**). As the transgenic allele utilizes a bidirectional *Thy1* promoter to drive neuronal expression of tamoxifen-inducible Cre^{ERT2} and EYFP, we first verified uniform expression of EYFP in DRG neurons (**Fig. S4a**). Crossing to the Rosa26-LSL-Sun1-GFP reporter line [41] also confirmed tagging of DRG neurons upon tamoxifen

injection (**Fig. S4b**). Genotyping showed excision of the *Ahr* floxed allele in DRG but not tail tissues from cKO mice at 2 weeks after tamoxifen injection (**Fig. S4c, d**), while RNA-seq demonstrated reduced mRNA reads of *Ahr* exon 2 (floxed region) in *Ahr*^{cKO} DRG relative to control (**Fig. S4e**). WB of DRG lysates from *Ahr* cKO mice still detected AhR immuno band likely from glial cells.

We next evaluated motosensory performance of adult mice after short term or long term *Ahr* deletion and detected comparable ladder walking with regular or irregular intervals and tactile perception by von Frey filament testing relative to control cohorts (**Fig. S4f-h, Supplementary Video S1, S2**). Hence, induced neuronal AhR ablation in adult mice did not appear to impair physiological nerve function in the time frames tested.

In congruence with results from *Ahr* cKO$^{Nestin\text{-}Cre}$ and AhR antagonist studies, neurite outgrowth assay showed that AhR-deficient DRG neurons from *Ahr* cKO mice also extended longer neurites at 24 hr post-seeding (mean length of 393 vs. 232 µm, a 70% increase) (**Fig. 2g**). The increased neurite length of *Ahr*-deficient DRG neurons did not reach that of conditioned DRG neurons, indicating that the conditioning lesion also operates through AhR-independent mechanisms.

The enhanced axon regeneration phenotype with *Ahr* cKO also held true for the in vivo sciatic nerve injury model, with more and longer SCG10^{+} regenerating axons extending beyond the crush site at both 1 dpi (longest axon length 869 vs. 594 µm, ~ 50% increase) and 3 dpi (5.8 vs. 4.8 mm, ~ 20% increase) (**Fig. 2i-j**). The regenerative phenotype at these early time points supports a priming effect of *Ahr* deletion for early initiation of regeneration gene programs.

We further conducted motosensory behavioral assays, which showed accelerated functional recovery of *Ahr* cKO mice relative to controls (**Fig. S5a-c**). At baseline, both genotypes displayed similar ability

to fully spread toes of the hindpaw, and sciatic nerve crush injury resulted in pronounced toe flexing and failure to bear weight on injured hindlimb in both cohorts (**Fig. S5b**). But by 9 dpi and at 13 and 17 dpi, *Ahr* cKO mice exhibited improved hindlimb toe spreading (**Fig. S5b, c**). The promoting effect of AhR cKO was also detected in an adult cohort with tamoxifen injected 14 months before nerve injury (**Fig. S5d-f**). Together, these results establish AhR as an inhibitor of axon regeneration; AhR deletion accelerated axon regrowth and functional recovery after peripheral nerve injury.

PL triggers an early induction of bHLH-PAS transcription factors in axotomized DRG

To better understand AhR signaling in the conditioning lesion paradigm [18,19], we analyzed DRG transcriptomes by RNA-seq [3], which revealed a positive gene set enrichment for both Xenobiotic metabolism and Hypoxia after PL (1 dpi) relative to naive state (**Fig. 3a, b, Table S1**). Consistently, RNA-seq revealed increased mRNA reads for both *Ahr* and *Hif1a* at 1 dpi (**Fig. 3c**). Time-course qRT-PCR analyses verified an early induction of *Ahr* and *Arnt* at 12 hr post-PL, which persisted at 48 hr; by comparison, *Hif1a* induction lagged slightly behind and was more transient, peaking at 24 hr and returning to baseline by 48 hr (**Fig. 3d**). In echo, data analysis of a recent single cell (sc)RNA-seq on conditioned DRG [42] also confirmed early induction of the three bHLH-PAS TFs (*Ahr, Hif1a, Arnt*) from 12 to 72 hr post-PL in many DRG neuron subtypes (**Fig. S6a**).

WB also demonstrated an early induction of AhR protein in axotomized DRG after PL: detectable as early as 2 hr, further increasing by 12 hr, peaking at 1-3 dpi, and persisting at 14 dpi. This pattern paralleled that of ATF3, a marker of the conditioning lesion [21] (**Fig. 3e, f**). HIF-1α induction/stabilization after PL also occurred early but appeared more transient: detectable at 12 hr (slightly preceding transcriptional changes), peaking at 1 dpi, but returning to baseline by 3 dpi (**Fig. 3e, f**).

As another sign of AhR activation, Cyp1b1 displayed an early but transient upregulation at 1 to 3 dpi, shown by WB, RNA-seq, and qRT-PCR time-course analyses, and the same was true for *Tiparp* (TCDD inducible poly(ADP-ribose) polymerase), another AhR target gene and a negative regulator of Ahr activity [43] (**Fig. 3e-g**, **S6b**). *Cyp1a1* and *Ahrr* showed low expression in DRG. AhR notably displayed an electrophoretic mobility shift after PL, particularly at 12 and 24 hr, similar to that by AhR agonist (shown in **Fig. 1f**). Hence, conditioning lesion seems to trigger an early but a transient AhR activation by endogenous ligands despite persistent elevation of AhR expression, in line with multiple feedback mechanisms to swiftly turn off AhR signaling [6]. Indeed, tamoxifen injection after sciatic nerve injury did not lead to axon regrowth advantage (**Fig. S6c**), illustrating an early role of AhR in response to axotomy.

AhR stability/cytoplasmic retention is controlled by cytoplasmic chaperones HSP90, XAP2 (AhR interacting protein, *Aip*), and p23 (Prostaglandin E Synthase, *Ptges3*) (**Fig. S7a**). RNA-seq showed a downregulation of *Aip* but not of *Ptgs3* or *Hsp90* at 1 dpi, while qRT-PCR detected a downregulation of both *Aip* and *Ptgs3* at 36 hr after PL (**Fig. S7b, c, Table S1**). These changes support an early AhR activation after PL. Attempts to detect AhR in DRG tissues by IHC did not yield specific immunosignals, thus precluding in vivo assessment of AhR nuclear translocation. Altogether, concurrent early induction of AhR and HIF-1α after axotomy likely set the stage for collaboration or competition to balance stress coping vs. axon regeneration (**Fig. 3h**).

Ahr activation can be controlled by the L-kynurenine metabolic pathway [44], and we thus examined our RNA-seq data for the expression of six biosynthesis enzymes involved in the conversion of tryptophan to L-Kyn or kynurenic acid, all showing no overt changes at 1 dpi (**Fig. S7d, e**). Time course qRT-PCR analysis revealed a downregulation of *Kyat1* but not *Kmo* at 36 hr, while an earlier gene matrix analysis [45] revealed low expression of *Ido1* and *Ido2* in DRG and only a modest downregulation of

Tdo2 at 3 dpi after PL (**Fig. S7f, g**). Hence potential alterations of endogenous AhR ligands in response to DRG axotomy likely originate from outside sources.

Since AhR ligand can be derived from gut microbiota [46], we treated mice with antibiotics to deplete gut microbiome [47], but no significant differences of axon regeneration was detected after sciatic nerve injury or in neurite outgrowth assay of DRG neurons (**Fig. S8a-d)**. Indole-3 propionate (IPA) has been reported to be a gut microbiota-derived metabolite in response to intermittent-fasting and promotes axon regeneration through neutrophil chemotaxis via pregnane X receptor (PXR) [48]. IPA has also been investigated as an AhR ligand that modulates sepsis and neuroinflammation [49,50], although the serum concentration of IPA is far below the levels needed to produce an AhR-dependent physiological effect [51]. Indeed, in neurite outgrowth assays, we observed that low or high doses of IPA resulted in no significant effect on control DRG neurons (in agreement with the report [48]) and even shorter neurites for *Ahr* cKO DRG neurons (**Fig. S8e**).

Since Thy1-Cre$^{ERT2/EYFP}$ may also be expressed by enteric neurons [52] (**Fig. S9a**), we examined gut epithelium and immune cell composition by IF, but found no overt differences between genotypes (**Fig. S9b, c**), concordant with a previous study [47].

AhR-dependent genes favor acute stress response and inflammation at expense of axonogenesis

Given the transcriptional roles of AhR and HIF-1α, we applied ChEA3, an integrative TF enrichment analysis tool that combines ChIP-seq datasets, gene co-expression, and TF-gene co-occurrence [53], on the regeneration-associated genes (RAGs) identified by our RNA-seq in conditioned DRG at 1 dpi relative to naive state (n=3,022; cutoff: $\log_2$FC>0.25, P<0.01) (**Fig. S10a**). This revealed 429 (14%) AhR-associated RAGs, including ATF3 and Jun, and 268 of them harbored AHRE in their promoter (**Fig. S10b, c, Table S2**). In comparison, ChEA3 identified 385 (13%) HIF-1α-associated RAGs,

including ATF3 and Jun, but also Gadd45a and IL6, and 144 of them harbored HRE in their promoter (**Fig. S11a-c, Table S3**).

Both AhR- and HIF-1α-associated RAGs featured shared but also distinct pathways related to acute stress response and axonogenesis. For instance, the 429 AhR-associated RAGs concerned xenobiotic metabolism (confirming AhR association), HIF signaling (signifying a link between AhR and HIF), axonogenesis, metabolism, stress responses, and immune trafficking (**Fig. S10d, e**). By comparison, the 385 HIF-1α-linked RAGs mainly concerned Hypoxia, Creatin metabolism, Circadian, Axon guidance Plexin D1, and BDNF signaling (**Fig. S11d, e**). There were 142 common genes linked to both AhR and HIF-1α (**Fig. S11g, Table S4**). Surveying a time-course gene matrix analysis of conditioned DRG [45] revealed that the majority of the RAGs linked to AhR, HIF-1α, or both were upregulated from 1 to 14 dpi (**Fig. S10f; S11f, h, Table S5 to S7**).

To further define the AhR regulon, we performed RNA-seq analysis on DRGs from control and *Ahr* cKO mice in naive state or after PL at 1 dpi (**Fig. 4a, Dataset 1**). This revealed 253 *Ahr* cKO DEGs in naive DRG (115 up- and 138 down-regulated), and 189 DEGs in PL axotomized DRG (73 up- and 116 down-regulated) (**Fig. 4b, c, S12a, b, Table S8, S9)**. Of the 253 DEGs in naive DRG, 156 (62%) harbored promoter AHRE, with the majority (83%) downregulated in cKO (likely direct targets of AhR), and 59 (23%) also harbored HRE (dually regulated by AhR and HIF-1α) (**Fig. S12c)**. Of the 189 DEGs in axotomized DRG, 80 (42%) contained promoter AHRE, 16 (8.5%) HRE, and 27 (14%) both, while 66 (37%) had no motif (**Fig. S12d**).

The downregulated DEGs in both naive and axotomized Ahr^{cKO} DRG were enriched for inflammation, albeit involving different pathways, e.g., interferon (IFN) and chemokines featured in naive DRG, complement and TNF in axotomized DRG (**Fig. 4d**, **e**). The upregulated DEGs in both states mainly

concerned neuronal functions (e.g., voltage-gated Ca^{2+} and K^{+} channels), with synapse organization and axonogenesis featured in naive DRG, G protein coupled receptor (GPCR) and carbohydrate biosynthesis in axotomized DRG (**Fig. 4d, e**). Ingenuity pathways analysis (IPA) further highlighted immune suppression and reduced stress as the main biological themes of *Ahr* ablation in both DRG conditions (**Fig. S12 g-h**). In addition, tryptophan degradation (confirming AhR regulation) and axonogenesis were featured in naive state, while HIF-1α signaling (a link between AhR and HIF) and carbohydrate metabolism were featured in axotomized state (**Fig. S12e-h**). Concordantly, GSEA showed that transcriptomes of *Ahr*^{cKO} DRG in both states share common negative enrichment for inflammation, Hypoxia, and ROS, and positive enrichment for Hedgehog signaling (**Fig. S13a, Table S10**).

To further assess the impact of *Ahr* ablation on transcriptional responses to axonal injury, we compared PL-induced RAGs in control DRG (n=3,022) vs. in *Ahr*^{cKO} DRG (n=3,183), with 2,066 overlapping genes (**Fig. 4f, Table S1, S11**). Comparative IPA again underscored a general suppression of stress response and immune signaling from *Ahr* ablation, but an augmentation of axon regenerative pathways such as GADD45, HIPPO, p53, DNA damage-induced 14-3-3 signaling (**Fig. 4f**).

As axonogenesis pathways were enriched in *Ahr*^{cKO} DRG, we next asked whether AhR ablation mimics the conditioning lesion in initiating regenerative gene programs. To this end, we intersected the 235 cKO DEGs in naive DRG with the PL-induced 3,022 RAGs in conditioned DRG at 1 dpi, revealing 61 overlapping genes (25%) that featured Axonal extension, DNA binding/transcription, Negative regulation of Wnt signaling (pro-axon regeneration [54,55]), and Retinoid metabolic process[56], etc. (**Fig. 4g, S13b, Table S12**). A heatmap analysis highlighted concordant transcriptional changes of 44 out of 61 genes between *Ahr* cKO and conditioning lesion, including 10 genes in the Axonogenesis GO terms (e.g., *Klf8, Ncam1, Hoxd11, Hoxc8*) (**Fig. 4g, S13c**).

Notably, *Ahr* cKO did not induce well-known RAGs in naive DRG, nor altering PL-triggered induction of these RAGs, including *Atf3, Smad1*, neurotrophins (*Bdnf, Ngf, Ntf3*), canonical HIF pathway genes (*Hif1a, Vegfa, Slc2a1*), or *Ppargc1a* (a master regulator of mitochondrial, glucose and fatty acid energy metabolism [57-59]), shown by both RNA-seq and qRT-PCR (**Fig. S13d, e**). Altogether, ablation of AhR in DRG partially mimics the conditioning lesion in launching axon regenerative gene programs but seems to involve novel gene pathways.

We next focused on the 189 cKO DEGs in axotomized DRG at 1 dpi. Intersection with 3,022 PL-RAGs revealed 49 common genes (i.e., AhR-dependent RAGs) concerning neuronal functions (e.g., Synapse long term depression, CREB signaling in neurons, Glutamate receptor signaling) and Phagosome Formation; by contrast, the 140 unique AhR-dependent genes mainly concerned inflammation, lipid, ECM, and HIF-1α signaling (**Fig. S14a, Table S13**). Heatmap comparison further illustrated a marked transcriptional impact of *Ahr* ablation on Phagosome Formation GO for both shared and unique categories (**Fig. S14a**); this also applied to 23 RAGs showing progressive expression changes from 3 to 14 dpi after PL [45] but discordant changes in Ahr^{cKO} (**Fig. S14b**). We also analyzed the predicted upstream regulators of the 189 DEGs in axotomized Ahr^{cKO} DRG, revealing regulators related to immune response (e.g., IRF2BP2, MALT1, IL17RA), metabolism (SRF, TCL1A, FOXO1), vascular regulation (AGT), and growth factor signaling (EGF, TGFA) (**Fig. S14c**). These results support a collaboration of AhR with diverse regulators in rewiring transcriptional networks.

While many similar pathways were enriched in both naive and axotomized Ahr^{cKO} DRG, particularly immune and stress response, there were only 7 common genes that regulate sugar and amino acid metabolism (Glutamine-fructose-6-phosphate transaminase 2 (*GFPT2*), Bisphosphoglycerate mutase (*BPGM*), immunity (Thy1; Immunoglobulin heavy constant gamma 3, *IGHG3*), secretion (Calcium

dependent secretion activator or *CADPS*), or epithelial tube formation (Multimerin 2 or MMRN2), WD repeat domain 72 (WDR72) (**Fig. S14d**). Further illustrating the distinct AhR regulons in naive vs. axotomized DRG, comparative IPA revealed that in the injury setting, *Ahr* cKO resulted in a wide suppression of neuroinflammation, neuronal function, and metabolic signaling, with exceptions of neurovascular coupling and lipid synthesis (LXR/RXR activation) (**Fig. S14e**). Hence, *Ahr* ablation exerted context-dependent transcriptional effects contingent on different DRG states. Indeed, RNA-seq on L4-6 DRGs from sham cohorts revealed 249 Ahr^{cKO} DEGs (148 up- and 101 down-regulated), concerning HIF1A (linking AhR and HIF), Spinal cord injury, BDNF, VEGF signaling, Synthesis of Lipoxins, and metabolisms, etc. (**Fig. S15a-c, Table S14, Dataset 2**). Further illustrating context-dependent effect of AhR ablation, only 8 DEGs were shared between naive and sham DRG and 21 DEGs between sham and PL DRG (reflecting response to general anesthesia, pain/stress, or axotomy), and notably four genes (*Cadps, Wdr72, Gfpt2* and *Thy1*) were AhR-dependent genes in all three DRG states (**Fig. S15d**).

Since ATF3 was a top RAG predicted to be associated with both AhR and HIF-1α by ChEA3 analysis, and contains AHRE in its promoter (**Fig. S16a, Table S2**), we further assessed the impact of *Ahr* ablation on ATF3 expression. WB revealed that *Ahr* cKO did not alter the low baseline expression of ATF3, nor its robust induction after PL (**Fig. S16b**). Consistently, IF showed that AhR deletion led to a slightly higher level of cytoplasmic ATF3 in naive DRG neurons, but no significant change of nuclear translocation in axotomized DRG (**Fig. S16c, d**). The levels of $pCREB^{S133}$ and GAP43 were not overtly changed in naive DRG, while pSmad1/5/8 showed a modest reduction relative to control (**Fig. S16c**).

We also examined the effects of in vivo administration of AhR agonist ITE, which induced transcription of genes containing promoter AHRE (*Atf3, Bdnf*) in naive DRG, but not genes without

AHRE (*Sprr1a, Gal, Npy, Csf1*) (**Fig. S16e, Table S2**). However, IF showed that in vivo ITE injection only led to higher cytoplasmic ATF3, while AhR antagonist TMF had no effect on ATF expression (**Fig. S16f**), but elevated pSmad1/5/8 and pS6K$^{Ser235/236}$ levels in naive DRG neurons (unlike *Ahr* cKO), consistent with higher axon growth potential (**Fig. S16g**). Hence, *Ahr* cKO and antagonist exerted convergent but also different effects on RAGs induction, contingent on duration of AhR inhibition and DRG states.

It is notable that even though inflammatory suppression was a main biological theme in *Ahr*^{cKO} DRG, IF showed no overt changes for CD45 (pan leukocyte marker), CD206 (anti-inflammatory myeloid marker), CD68 (phagocytic marker), IBA1 (myeloid marker upregulated in activated macrophages), or PU.1 (myeloid lineage marker) in naive or axotomized DRG (**Fig. S17a, b**). IF for other immune cell markers revealed scant numbers of NK1.1 (NK cells), Ly6G (neutrophils), CD4 or CD8 T cells in naive or axotomized DRGs. Additionally, at the injury site of crushed sciatic nerves, the number and distribution of macrophages (F4/80^{+}) and Schwann cells (Sox10^{+}) appeared comparable between genotypes (**Fig. S18a-b**). Hence the impact of AhR ablation on inflammatory suppression was not simply reflected by the immune cell compositions in axotomized DRG or injured nerves.

Axon growth promoting effect of AhR ablation requires HIF-1α, while absence of Arnt does not affect axon regrowth capacity

Since AhR ablation is expected to increase the availability of Arnt for dimerizing with HIF-1α, we expected enhanced HIF signaling by *Ahr* deletion. However, GSEA revealed that while PL led to a positive enrichment of Hypoxia gene set in both control and *Ahr*^{cKO} DRG, *Ahr* ablation in fact resulted in an overall negative enrichment of Hypoxia gene set in both naive and axotomized DRG (**Fig. S19a**).

We further examined the 196 genes in the Hallmark_Hypoxia gene set, which displayed a complex

transcriptional pattern on individual gene level, with many genes downregulated after PL (even though the Hypoxia gene set was positively enriched) (**Fig. S19b, Table S15**). PL clearly exerted a stronger transcriptional effect on these genes as compared to the modulatory effect of *Ahr* deletion (**Fig. S19b**). Venn diagram revealed few overlapping genes between *Ahr* cKO DEGs (in naive or axotomized DRG) with the Hallmark_Hypoxia genes, HIF-1α dependent signature genes [4] (n=493, with 108 (22%) overlapping with the PL-RAGs), or the 385 predicted HIF-associated RAGs (**Fig. S19c, d**, **Table S16**). Taken together, *Ahr* deletion led to an overall suppression of HIF signaling, suggesting collaboration rather than antagonism of the two in the setting of axonal injury.

We next focused on the functional relationship of AhR and HIF signaling. To this end, we treated DRG neurons with KC7F2, a specific inhibitor of HIF-1α protein synthesis via pS6K inhibition [60]. IF confirmed reduced HIF-1α in KC7F2-treated DRG neurons after DMOG exposure (to augment HIF1a levels) (**Fig. S19e**). KC7F2 resulted in a reversal of the axon promoting phenotype of *Ahr* deletion (**Fig. 5a-c**). We next tested conditioned DRG neurons (PL 3 days prior), which exhibited enhanced axon growth potential, with mean longest neurite length reaching 274 µm by 12 hr after plating. Remarkably, *Ahr* deletion further augmented the conditioning effect (with longest neurites reaching mean length of 326 µm, a 20% increase), and this was again diminished with KC7F2 treatment (**Fig. 5d-f**). In aggregate, the growth advantage of AhR-deficient DRG neurons appear to require HIF-1α.

Arnt is a common β unit for both AhR and HIF-1α. Since both Xenobiotic metabolism and Hypoxia gene sets were enriched in DRG after PL, we next tested the impact of *Arnt* cKO (*Arnt*$^{fl/fl}$ Thy1-Cre$^{ERT2/EYFP}$, confirmed by qRT-PCR) (**Fig. S20a**). *Arnt*-deficient DRG neurons extended comparable length of axons as controls (**Fig. 5g-i**), with no further effect from HIF inhibition by KC7F2 or HIF activation by hypoxia exposure (**Fig. S20b-c**). Likewise, conditioned neurons exhibited similar axonal length regardless of genotype or oxygen tension (**Fig. 5h-i, S20c**). In line with the in vitro data, the in

vivo sciatic nerve injury model also showed that the extent of regenerating axons ($SCG10^+$) in *Arnt* mutant mice matched that in littermate controls at 3 dpi (maximal mean length 4.6 ± 0.3 vs. 4.7 ± 0.4 mm) (**Fig. 5j-l**). Hence, in the absence of Arnt, DRG neurons were able to mount a successful axon regeneration relying on other mechanisms (**Fig. 5m**).

TFs often collaborate with chromatin regulators to rewire gene circuits through epigenetic reconfiguration [61,62]. Our previous genome-wide profiling of differential DNA hydroxymethylated regions (DhMRs) after DRG axotomy identified 1,036 PL-specific DhMRs at 1 dpi, mostly residing in gene bodies or non-coding regions (**Fig. S21a, b**) [3,62]. Interestingly, PL-DhMRs are enriched for binding motifs of many bHLH-PAS TFs, including Bmal1, Clock, HIF-1α, and Arnt, but not AhR [3]. In fact, 40% of the PL-DhMRs (436) contained HRE motif, corresponding to 766 associated genes, and 169 of them intersected with PL-RAGs, featuring Circadian Rhythm (linking HIF and Bmal1) and notably Neurotrophin/Tyrosine kinase receptor pathway (**Fig. S21c, d; Table S17, S18**). Among the 169 genes harboring PL-DhMR/HRE, 19 were shared with the *Ahr* cKO DEGs in naive DRG and 8 in axotomized DRG (**Fig. S21e**). Thus, AhR-regulated DEGs may operate through DhMR/HRE residing mostly at gene bodies, rather than promoters [3,62].

Further linking AhR and 5hmC, *Ahr* deletion also affected the GADD45 pathway (see **Fig. 4f**), which is linked to DNA demethylation, and 5hmC levels appeared higher in axotomized *Ahr cKO* $^{nes\text{-}cre}$ DRG neurons (**Fig. S21f**). Our recent study showed that circadian regulator Bmal1 gates regenerative responses of DRG neurons partly through 5hmC gain [3]. Interestingly, xenobiotic metabolism and AhR signaling were the top enriched pathways of the *Bmal1* cKO regulon upon PL (**Fig. S21g, h)**. This implied Bmal1 as a potential upstream regulator of AhR signaling, and that Bmal1, AhR, and HIF-1α are three interconnected bHLH-PAS TFs for different transcriptional tasks in preparing DRG for axonal injury (**Fig. S21i**).

AhR antagonist induces RAGs and regulators of RNA Polymerase III and ISR after axotomy

So far, we showed that *Ahr* cKO was able to rewire transcriptional circuits in both naive and axotomized DRG that correspond to enhanced axon growth. To evaluate translational relevance, we tested pharmacological manipulation of AhR activity shortly after axotomy by delivering drugs at 1 hr after PL and then daily at 1 and 2 dpi (**Fig. 6a**). Unlike gene ablation or AhR agents delivered in the absence of axonal injury, post-injury injection of AhR antagonist TMF led to augmented induction of well-known RAGs in axotomized DRG analyzed at 3 dpi, including *Bdnf, Atf3, Sprr1a, Gal,* and *Npy,* while an AhR agonist exerted no overt effect (**Fig. 6b**). These results support a repressive role of AhR for PL-induced RAGs induction, which can be alleviated by pharmacological targeting of AhR delivered after PL.

We then explored the efficacy of this regimen in a sciatic nerve crush injury model with the AhR antagonists SR1 and Bay2416942 (Bay), both in clinical development [63]. Similar to the results of tamoxifen injection after injury in *Ahr* cKO cohorts, post-injury delivery of SR1 or Bay did not accelerate axon regrowth, even though the contralateral DRG neurons prepared from the same mice treated with Bay extended longer neurites (**Fig. S22a-c**). This may reflect suboptimal drug dosage or treatment duration and the importance of early priming from AhR inhibition to achieve faster axon regrowth over the already robust regeneration in the sciatic nerve crush model. Encouragingly, as a proof-of-principle in a severe thoracic_spinal cord injury model, we observed that mice treated with SR1 (either with low or high dose starting at 4 hr after SCI and then continued daily) showed improved motosensory functional recovery when compared to vehicle control, beginning from 28 dpi (BMS sub-scores started improving at 14 dpi) and onward until 49 dpi (**Fig. S22d, e)**.

Systemic delivery of AhR antagonist can affect neurons but also glial cells. Indeed, analysis of the

injured Sciatic Nerve Atlas (iSNAT) [64] revealed high levels of *Ahr* transcripts in Schwann cells at baseline, as well as in activated Schwann cells, immune cells, and endothelial cells after nerve injury (**Fig. S22f**). Query of a scRNA-seq dataset on axotomized DRG [65] also detected *Ahr* transcripts in satellite glial cells, macrophages, and endothelial cells (**Fig. S22g**), although in primary DRG cultures, we detected significantly higher AhR protein levels in DRG neurons than in Schwann cells ($SOX10^+$) (**Fig. S22h**). Thus, a glial effect [66] may contribute to the different regenerative phenotypes between *Ahr* cKO and AhR antagonists.

To better understand neuronal effects of AhR ablation, we conducted RNA-seq on semi-purified DRG neurons from *Ahr* cKO vs. control mice after 24 hr culture (axotomized during dissociation). This revealed 408 DEGs (262 up-, 146 down-regulated) featuring AhR pathway (confirming cKO), Hypoxia and Angiogenesis (linking AhR and HIF), Circadian Entrainment (linking AhR and Bmal1), as well as Spinal cord Injury and Axonogenesis (**Fig. 6c; Fig. S23a-c, Dataset 3**). The upregulated DEGs concerned axonogenesis-related pathways such as Neurotrophin binding, Transmembrane RTK activator, Forskolin, and Filopodium membrane, while the downregulated DEGs prominently featured GO of RNA regulation and Metabolic signaling (**Fig. 6d**).

We next leveraged a published dataset of scRNA-seq of DRG neurons to further define the AhR regulon in response to PL [67], revealing 98 AhR-associated genes (**Fig. 6e; Table S19**). Notably, pooled scRNA-seq results from 6 hr, 1, 2, 7, 14 dpi predicted inactivation of AhR after PL (in agreement with our model of a transient activation of AhR signaling), in contrast to general activation of well-known regeneration-associated TFs such as ATF3, Sox11, Smad1, Creb1, Myc, Jun, as well as ERG (Egr1, Fos) (**Fig. S24a**). Pathway analysis of the 98 AhR-associated genes again highlighted RNA Polymerases (Pol) regulation (e.g., RNA Pol III transcriptional termination, regulation of transcription by RNA Pol II, Negative regulation of pri-miRNA RNA Pol II) (**Fig. 6f**), echoing our RNA-seq

findings in semi-purified DRG neurons.

RNA Pol III transcribes small RNAs including transfer (t)RNA and S5 ribosomal (r)RNA [68], potentially impacting global protein translation. We next assessed the impact of in vivo pharmacological manipulation of AhR on *Nfia* and *Nfib*, two genes involved in transcriptional termination of RNA Pol III and both containing AHRE in their promoter. We found that AhR antagonist TMF downregulated *Nfia* and *Nfib*, whereas agonist ITE had no effect (**Fig. 6g, S24b**). We also analyzed genes of GO terms enriched in these 98 AhR-associated genes and found that *Sox9* and *Rest* (negative regulation of neural differentiation GO) and *Cdk6* (gliogenesis), all containing AHRE and HRE in promoter, as well as *Stmn* (encoding SCG10, a widely used marker of sensory axon regeneration) showed upregulation by TMF but were not affected by ITE upon PL (**Fig. S24d**).

Finally, analysis of scRNA-seq data of axotomized DRG [67] also showed activation of a number of TFs acting as sensors in ISR, e.g., ATF4, ATF6, and Ddit3 [69] (**Fig. 6d)**. Intriguingly, *Atf4*, a TF activated by increased cellular levels of uncharged tRNA [70], harbors AHRE in promoter and it was induced early after PL in a majority of DRG neurons subtypes (**Fig. S24a, c**). Further assessment of the impact of AhR inhibition by TMF on these ISR regulators revealed a general downregulation (**Fig. 6g**), signifying that AhR inhibition partly operates through repression of ISR.

Discussion

Injured neurons need to respond to environmental stressors while balancing regenerative needs. Here, we uncovered a role of AhR in engaging tissue-protective gene networks for xenobiotic metabolism, inflammation, and ISR, but at the expense of axon regeneration. AhR inhibition can shift the balance towards regenerative gene programs to accelerate axon regeneration (**Fig. 6h**).

All organisms are continuously exposed to external chemicals, known as xenobiotics, and xenobiotic detoxification systems emerged early in evolution as a protective mechanism, mainly through metabolizing enzymes and transporters to mitigate toxicity. AhR is well known for its involvement in toxicology and carcinogenesis; its neuronal functions are less well-defined, even though AhR is widely expressed in the nervous system (in invertebrates almost exclusively in neurons) [71,72]. The detoxification function of AhR may be a late evolutionary adaptation, in contrast to its central role in neural homeostasis, synaptic function, and cell fate specification [71]. Genetic disruption of *Ahr* homologs in *C. elegans* or in *Drosophila* affected axon and dendritic branching [72,73]. Similarly, *Ahr* deletion in mouse led to increased dendrite branching and spine density of hippocampal neurons, affecting learning and memory [74]; *Ahr* cKO in cerebellar granule neuron precursors promoted differentiation and neurite outgrowth [75]. Our current study thus extends the neuronal functions of AhR as a key regulator of axonal injury response. In echo, an unbiased high throughput screen combined with analysis of TF binding sites computationally predicted AhR as a regulator of axon growth [76] .

Axon regeneration requires concerted transcriptional regulation to induce RAGs. Previously, we and others have identified a set of regeneration-associated TFs [20,45,77,78] and epigenetic regulators [62,79,80] in conditioned DRG, but their functional diversity, collaboration vs. antagonism, downstream targets, and epigenetic links remain opaque. Here, we showed responsiveness of DRG neurons to ligand-mediated

AhR signaling, evidenced by cytoplasm-nuclear shuttling of AhR and transcriptional changes of canonical detox target genes (*Cyp1a1* and *Cyp1b1*). Peripheral nerve lesion resulted in early induction of AhR and HIF-1α, fitting with gene set enrichment for both xenobiotic metabolism and hypoxia in DRG transcriptomes at 1 dpi. As a transcription factor, AhR controls a large repertoire of target genes via AHRE, as well as second-wave downstream genes regulating a wide range of biological processes. AhR activation appeared to be transient despite prolonged elevation of protein levels, consistent with multiple negative feedback mechanisms including induction of Cyp1 enzymes to degrade AhR ligands, upregulation of AhRR to compete for Arnt and for AHRE occupancy, downregulating Kyat1 to limit production of local AhR ligands, and induction of HIF-1α. In addition, ligand-activated AhR is also subject to ubiquitination and proteasomal degradation [6]. The transient nature of AhR activation is not only important to prevent detrimental AhR overactivity, but also for timely release of Arnt for HIF signaling; vice versa, the promoting effect of intermittent hypoxia [4] may operate through competition with AhR for Arnt binding.

While functional assays suggested that the growth advantage of *Ahr*^{cKO} DRG neurons required HIF-1α, the signaling relationship between the two pathways appears complex, reflected by overall collaboration, but antagonism on individual gene level. In this context, HRE-driven genes as a result of *Ahr* cKO (e.g., neurotrophin pathway genes) may operate through PL-DhMR/HRE (residing in gene bodies) and not via HRE in promoter (as in Hypoxia signature genes). Apart from Arnt, AhR may also regulate non-AHRE containing genes through interaction with other factors [81].

Our comparative transcriptomics unveiled the molecular underpinning of the growth promoting phenotype of *Ahr* deletion, highlighting suppression of acute stress and inflammation, in line with the well-documented function of AhR as an environmental sensor for dietary metabolites/pollutants/injury metabolites to upregulate detoxification enzymes and mediator of oxidative stress response [6]. *Ahr* cKO

launches axonogenesis gene programs, consistent with accelerated axon regeneration after PL at early timepoints of 1 to 3 dpi. Interestingly, the DEGs did not include well-known RAGs such as *Atf3*, *Npy*, *Gap43*, but instead involved new pathways such as Phagosome formation and carbohydrate metabolism, while AhR-dependent genes in DRG neurons featured regulation of RNA polymerase III and ISR.

Our data also revealed the interconnectedness of bHLH-PAS TFs in regulating axonal regenerative responses, linking circadian (Bmal1) [3], hypoxia (HIF), and xenobiotic metabolism/acute stress (AhR), each controlling distinct but also shared target genes. Bmal1 appeared to be an upstream regulator of AhR/xenobiotic pathways, while HIF also controls circadian pathways [82]. Our studies also identified a link of bHLH-PAS TFs with DNA hydroxymethylation after PL. Indeed, exposure to AhR ligands can lead to methylation changes around AHRE [83]; in echo, GADD45 is among the DEGs of AhR cKO, along with 5hmC gain in axotomized DRG neurons. Hence, AhR may alter transcription also by modulating DNA (hydroxy)methylation.

From a therapeutic point of view, we demonstrated that in vivo administration of AhR antagonist after the onset of axotomy induced RAGs such as *Bdnf*, *Atf3*, *Sprr1a*, *Gal1* and *Npy* (unlike in non-injury setting or *Ahr* genetic ablation). Hence, the effect of AhR antagonist on gene expression is influenced by the duration of AhR inhibition, temporal relationship to axonal injury, and the abundance or potency of endogenous AhR ligands. The sources and identity of AhR endobiotic (endogenous compounds) or xenobiotic ligands (a.k.a xenokines) or proligands may be difficult to identify, as injury metabolites may arise locally inside axotomized DRGs or originate via circulation from systemic inflammation. We tested antibiotics treatment to deplete AhR ligands derived from gut microbiome but detected no overt effects in our models. While enteric neurons presumably are also affected by neuronal *Ahr* cKO, we also detected no apparent changes of the immune composition, although an

effect of gut-licensed immune cells infiltrating axotomized DRG or nerve injury site cannot be excluded. Future studies are needed to test the efficacy of AhR antagonist delivered at a particular time window and optimal dosage to accelerate nerve repair. In this context, the function of AhR antagonist may dependent on endogenous ligands [31] and high dosage of AhR antagonists may have partial agonistic activity [84]. AhR can also be activated by oxidative stress, independent of ligands [85].

Echoing our findings, inhibition of AhR also has beneficial effects for CNS diseases such as stroke, wherein *Ahr* deletion or antagonist led to reduced infarct volume and gliosis, along with improved motosensory recovery [86]. In a Huntington's disease model, *Ahr* deletion protects against neurotoxicity and oxidative stress [87]. Recent studies also reported a protective function of AhR in the gut-lung axis [88] and the role of endothelial AhR signaling in integrating dietary cues to maintain tissue homeostasis [89]. AhR is also important for timely termination of the regenerative response of intestinal epithelia [90]. There also exists naturally occurring AhR polymorphism within and across species, leading to differences in the sensitivity and response to AhR ligands [6]; whether that might lead to different axon regenerative capacity and whether different dietary regimens or unique pathogen loads would be a factor awaits future studies. Also notable is that constitutive expression of *Cyp1a1* gene partially phenocopies *Ahr* null phenotype by reducing cognate ligand of AhR [9], thus offering an alternative way to modulate AhR activity.

In summary, our studies provide new understandings of an antagonizing role of AhR for axon regeneration and crosstalk with HIF and epigenetic mechanisms, thus opening new strategies to enhance axon regeneration and nerve repair.

Methods

Animals

All animal studies were performed under protocols approved by the Institutional Animal Care and Use Committee (IACUC) at Icahn School of Medicine at Mount Sinai. Animals were housed in a pathogen-free barrier facility, under a 12-hour light: dark cycle with food and water provided *ad libitum*.

C57BL/6J mice (JAX stock no. 000664), *Ahr*$^{fl/fl}$ mice (*Ahr*$^{tm3.1Bra}$/J; stock no. 006203), Nestin-Cre mice (B6.Cg-Tg(Nes-cre)1Kln/J; stock no. 003771), Thy1-CreER^{T2} mice (Tg(Thy1-cre/ERT2,-EYFP)HGfng/PyngJ; stock no. 012708), and Rosa26^{INTACT} mice (B6;129-Gt(ROSA)26Sor$^{tm5(CAG-Sun1/sfGFP)Nat}$/J; stock no. 021039) were obtained from Jackson Laboratory. *Arnt*$^{fl/fl}$ mice were obtained from Frank Gonzalez, NIH. All mice were bred on a C57BL/6J genetic background. Littermates were used as controls.

The following primers were used for genotyping by PCR using mouse tail DNA:

Ahr$^{fl/fl}$ mice: F1: GTCACTCAGCATTACACTTTCTA, F2: CAGTGGGAATAAGGCAAGAGTGA, R1: GGTACAAGTGCACATGCCTGC. Expected band sizes: 106 bp for wildtype allele, 140 bp for floxed allele, and 180 bp for excised floxed allele.

Arnt$^{fl/fl}$ mice: F1: TGCCAACATGTGCCACCATGT, R1: GTGAGGCAGATTTCTTCCATGCTC. 290 bp for wild type allele, 340 bp for Arnt floxed allele.

Nestin-Cre mice: F1: CCGCTTCCGCTGGGTCACTGT, R1: TGAGCAGCTGGTTCTGCTCCT, R2: ACCGGCAAACGGACAGAAGCA. 379 bp for wild type allele, 229 bp for transgenic Cre allele.

Rosa26^{INTACT} mice: F1: GCACTTGCTCTCCCAAAGTC, R1: CATAGTCTAACTCGCGACACTG, R2: GTTATGTAACGCGGAACTCC. 557 bp for wild type allele, 300 bp for knockin allele.

Thy1-CreER^{T2} mice: F1: TCTGAGTGGCAAAGGACCTTAGG,

R1: CGCTGAACTTGTGGCCGTTTACG, Int-F2: CAAATGTTGCTTGTCTGGTG, Int-R2: GTCAGTCGAGTGCACAGTTT. 200 bp for wild type allele, 300 bp for transgenic Cre allele.

In vivo drug treatments

For conditional knockout, tamoxifen (Sigma T5648), dissolved in corn oil (Sigma C8267), was injected intraperitoneally (100 mg/kg) once daily for 5 days. For AhR agonist or antagonist treatment, 2-(1′H-indole-3′-carbonyl)-thiazole-4-carboxylic acid methyl ester (ITE, Tocris 1803) or 6,2',4'-Trimethoxyflavone (TMF, Tocris 3859) were reconstituted in DMSO and further diluted in 12.5% kolliphore/PBS (Sigma C1535) to a final volume of 600 µl. Similar preparation was made with DMSO as vehicle control. Both drugs were injected intraperitoneally (10 mg/kg) as specified in the experimental paradigm. StemRegenin1 (SR1; Selleckchem S2858) and Bay2416964 (Selleckchem S8995) were reconstituted in DMSO and injected intraperitoneally (25 mg/kg) using a Hamilton fine syringe (Hamilton 80920).

Antibiotics treatment was performed according to previous study with modification [47]. Wild-type C57BL/6J mice received drinking water containing 1 g/l ampicillin sodium (Sigma A9518), 0.5 g/l vancomycin hydrochloride (Sigma V2002), 1 g/l neomycin sulphate (Sigma N1876), 1 g/l metronidazole (Sigma M1547), 50g/l sucrose (Sigma S0389), and 4 mM Acetic acid for 18 days before sciatic nerve crush. Light protected bottles were used and changed every third day.

Sciatic nerve lesion

Male and female mice, age 8-18 weeks old unless otherwise specified, were anesthetized by isoflurane inhalation (5% for induction, 2% for maintenance). A small skin incision was made at mid-thigh using a scalpel blade after skin preparation and disinfection. To clearly expose the sciatic nerve, the fascial space between biceps femoris and gluteus superficialis muscles was opened gently without

hemorrhage. The nerve was then freed from surrounding connective tissue under microscope, avoiding shearing or traction force. For sciatic nerve crush model, the nerve was crushed with an Ultra-fine Hemostat (Fine Science Tools 13020-12) for 15 sec at the third click. For sciatic nerve transection model, the nerve was cut with a 3 mm Vannas Spring Scissor (Fine Science Tools 15000-00). For sham surgery, the sciatic nerve was exposed as described but left intact. Mouse skin was closed with Reflex 7 mm Wound Closure System (Braintree Scientific RF7 CS) after surgery. Mice were left to recover in a warm cage. All surgical instruments were autoclaved before surgery and principles of asepsis were maintained throughout.

Spinal cord injury model

All procedures were conducted according to the protocol approved by the Institutional Review Board/Animal Ethics Committee of Texas A&M University (IACUC 2018-0324). T7-T9 laminectomy was performed on 8-week-old mice (wild-type C57Bl/6NJ male). The mice were then clamped using 2 pairs of Adson forceps before using the Infinite Horizon Impactor at 50 kdyn of force with a 2 sec dwell time to induce a severe T8 contusion and compression as described [91]. The muscles and skin were secured with 5.0 sutures and the skin was sealed with Dermabond. Buprenorphine SR-LAB (1 mg/kg) and Penicillin (100,000 units/kg) were injected subcutaneously once immediately post-surgery to prevent postoperative pain and infection. After surgery, mice recovered in a warmed cage and then moved to a normally temperate cage and provided with food and water ad libitum. All surgeries were performed in the morning (8am - 12pm) to limit potential circadian influence. Bladders were expressed manually twice daily. All groups, including the vehicle group, received once daily intraperitoneal (i.p.) in 100% dimethyl sulfoxide (DMSO) solution at 0.6 mL/kg as the vehicle. StemRegenin1 (SR1) was purchased lyophilized (TargetMol, Catalog No. T1831). SR1 was dissolved in 100% DMSO (Fisher Scientific, Catalog No. ICN19481983). Drug administration began 4 hours post injury and continued

daily for the entire duration of the experiment. All administrations were done by individuals blinded to experimental groups.

Primary DRG neuron culture

Adult DRGs from adult C57BL/6J mice were dissected and placed in ice-cold DMEM/F12 (Gibco 11330057). DRGs were washed 3 times with ice-cold calcium- and magnesium-free HBSS (Gibco 14175095) including 10 mM HEPES (Gibco 15630106) before incubating in 0.3% collagenase I (Worthington LS004196) for 90 min at 37°C. DRGs were then washed 3 times with HBSS buffer with HEPES at room temperature, followed by additional digestion in 0.25% trypsin-EDTA (Gibco 25200072) containing 50 μg/ml DNase I (Worthington LK003172) for 30 min at 37°C. Trypsinization was stopped with warm DMEM medium (Gibco 10569044) containing 10% FBS (Gibco 26140079) and DNase I. DRGs were dissociated by trituration with fire-polished Pasteur glass pipets (Fisherbrand 13-678-20D). To remove myelin debris and cell clumps, a partial-purification step was performed by centrifugation through a BSA (Fisher BP9700100) cushion. Specifically, the DRG suspension was mixed with 8 ml NS-A Basal Medium (NeuroCult 05750) and then 2 ml of 15% BSA in HBSS was added at the bottom of the 15 ml centrifuge tube followed by centrifugation at 1,000 rpm for 6 min. Supernatant was carefully removed and DRG were resuspended in NS-A Basal medium containing 2% B27 (Gibco A3582801), 0.725% Glucose, 0.5mM L-Glutamine, and 0.4% Antibiotic-Antimycotic (Gibco 15240062). DRG neurons were plated on Poly-L-ornithine (Sigma P4957) and laminin (Gibco 23017015) coated chamber slides or 6-well plates for subsequent experiments.

Generation of induced human neurons

The studies using hESCs were approved by the Embryonic Stem Cell Research Oversight Committee (ESCRO) at Icahn School of Medicine at Mount Sinai. Induced neurons were generated as described [3]. Briefly, H9 cells were obtained from the Mount Sinai Stem Cell Core, passaged, and maintained in

mTeSR1 media (Stem Cell Technologies #85850). To avoid contamination, antibiotic-antimycotic agent was added at 0.4% to all media (Gibco 15240062).

Induction of neuroprogenitor cells (NPCs) was performed using STEMDiff SMADi neural induction kit (Stem Cell Technologies 08581) as instructed. Stem cell colonies were seeded at a density of 3 $x10^6$ cells/ml in STEMDiff SMADi media supplemented with 2.5 mM thiazovivin (Calbiochem 420220). AggreWell 800 plate (Stem Cell Technologies 34850) were used for EB induction. On day 5, EBs were replated in 6-well plates precoated with Matrigel (Corning 356238), and full media changes were performed daily. Neural rosettes were selected on day 12 using STEMdiff Neural Rosette Selection Reagent (Stem Cell Technologies 05832) and replated daily full media changes until 80% confluence. The resulting NPCs were passaged at a density of 1.2 $x10^6$ in 2 ml in STEMdiff Neural Progenitor Medium (Stem Cell Technologies 05833). NPCs fate was confirmed by immunostaining for Nestin and Pax6.

Mixed cortical neurons culture was induced from NPCs as described [92]. NPCs were seeded in at 360,000 cell/well in differentiation media containing BrainPhys media (StemCell Technologies 05790) with 1x N2 (Gibco 17502048), 1x B27 (Invitrogen 12587-010), 20 ng/ml brain-derived neurotrophic factor (BDNF, Peprotech 450-02), 20 ng/ml glia-derived neurotrophic factor (GDNF, Peprotech 450-10), 200 µM L-ascorbic acid (Stem cell technologies 72132), and 250 µg/ml dibutyryl cyclic AMP sodium salt (db-cAMP, Stem Cell Technologies 73884). Half the media volume was changed with fresh differentiation media every other day for 10 to 13 days before analysis.

Mouse adult cortical neuron isolation

Cortical neuron assay was conducted as described [33]. Briefly, wild-type 6-week-old C57BL/6NJ male mice were euthanized using CO_2 and the cortex was isolated and transferred to a MACS C-tube, then dissociated using the Miltenyi gentleMACS octo-dissociator on a preset protocol. This was followed

by the removal of debris and endothelial blood cells using the Mitlenyi MACS Adult Brain Dissociation Kit (Miltenyi Biotec 130-107-677). Next, using the Adult Neuron Isolation Kit (Miltenyi Biotec 130-126-603), following manufacturer's instructions, the negative fraction (fraction enriched with neurons) was collected and used for the cortical neurite outgrowth assay.

Neurite outgrowth assays

L4-L6 DRG neurons were seeded on pre-coated 4-well chambered slides (Falcon 10384501), at ~1,000-2,000 neurons per well. Neurons were fixed with ice-cold 4% PFA and stained with anti-Tubulin β3 to visualize regenerating neurites.

For pharmacological experiments, DRG neurons from wild-type C57BL/6J mice were plated on pre-coated 6-well plate, using neurons from 8-10 DRG per well. Neurons were cultured for 24 hr with endogenous AhR agonists 2-(1′H-indole-3′-carbonyl)-thiazole-4-carboxylic acid methyl ester (ITE, Tocris 1803), L-Kynurenine (Tocris 4393), or antagonist CH 223191 (Tocris 3858) at the indicated concentrations. All drugs were dissolved in DMSO. Cells were fixed for immunofluorescence staining or used for qRT-PCR analysis.

A replating assay was performed on induced neurons between differentiation day 10 to 13 as described [3,93]. Briefly, cells were washed 2X with PBS and incubated in 0.025% trypsin for 5 min at 37 °C. Trypsin was gentle removed while keeping neurons attached and replaced with differentiation media. Gentle pipetting was then carried out to dissociate the neurons followed by counting and seeding in 4-well chamber slides at a density of 55,000 cells/well in differentiation media containing Ahr agonists: 6-Formylindolo[3,2-b]carbazole (Tocris, 5304), 2-(1′H-indole-3′-carbonyl)-thiazole-4-carboxylic acid methyl ester (Tocris, 1803), L-Kynurenine (Tocris, 4393), Norisoboldine (Selleckchem, s9092), or antagonists: CH 223191 (Tocris, 3858), 6,2',4'-Trimethoxyflavone (Tocris, 3859), StemRegenin1

(Selleckchem, S2858) for 1 day before analysis. All drugs were dissolved in DMSO, aliquoted, and stored at -80 °C.

Adult mouse cortical neurite outgrowth assay was performed as described [33]. Briefly, primary adult cortical neurons were seeded onto PDL coated plastic bottom plates (Greiner-Bio 781091) at 10,000 cells/well for 2 days. StemRegenin1 (SR1, TargetMol T1831) and vehicle were added at the time of plating and left in the media for 2 days without media change. Neuronal media consists of MACS Neuro Media (Miltenyi Biotec 130-093-570), 2 mM L-alanine-L-glutamine dipeptide (Sigma-Aldrich G8541-100ML), and 1×□B-27™ Plus Supplement (ThermoFisher A3582801).

qRT-PCR

Total RNA of cells or tissues was extracted with RNeasy Plus Mini kit (QIAGEN 74134). For RNA collection from tissue, dissected DRGs were initially stored in RNAlater Stabilization Solution (Invitrogen AM7024), and then homogenized in RLT Plus buffer including 1% β-mercaptoehanol using RNase-free disposable pellet pestles (Fisherbrand 12-141-364). For RNA collection from cells, cell cultures were washed once with PBS and then lysed by vigorous pipetting. Genomic DNA was eliminated through a gDNA eliminator column according to the manufacturer's instructions. RNA was eluted in RNase-free water and stored at -80°C. cDNA was prepared with the SuperScript III First-Strand Synthesis System (Invitrogen 18080051) from equal amounts of RNA (approximately 200 ng from DRG tissues and 500 ng from cell culture for each reaction). Quantitative RT-PCR (qRT-PCR) was performed with PerfeCTa SYBR Green FastMix Rox (Quanta Bioscience 95073-012) with an ABI 7900HT quantitative PCR system (Applied Biosystems) at the Mount Sinai qPCR CoRE. *Hprt1* was used as the house-keeping gene to normalize qRT-PCR results. PCR primers are listed in supplemental **Table S20**.

Western blot

L4-L6 DRG were collected and immediately frozen in liquid nitrogen and stored at -80°C for later analysis. Tissues were homogenized and lysed with RIPA buffer (Sigma R0278) containing EDTA-free protease inhibitor cocktail (Roche 04693159001) and phosSTOP (Roche 4906845001). The frozen DRG in a 1.5 ml tube were disrupted with RNase-free disposable pellet pestles (Fisherbrand 12-141-364) on ice. 1 U/µl benzonase nuclease (Millipore E1014) was added to lysis buffer. Samples were mixed on a rotator at 4°C for 30 min and then spun in a tabletop centrifuge at 13,000 rpm for 10 min to remove tissue pellet. An equal volume of 4x LDS sample buffer (Invitrogen NP0008) was added to lysates, which were then boiled at 95°C for 5 min. Lysate from equal number of DRGs was loaded and separated by electrophoresis on 4-12% ExpressPlus gels (Genscript M41210), followed by transfer to a PVDF membrane. Membranes were blocked in Intercept Blocking Buffer (LI-COR Biosciences 927-70001) at room temperature for 1 hr and subsequently incubated with primary antibodies diluted with Intercept Antibody Diluent (LI-COR Biosciences 927-75001) at 4°C overnight. Blots were washed with PBST (5 x 5 min) and incubated with secondary antibodies at room temperature for 1 hr. Bands were detected with the Odyssey Infrared Imaging System (LI-COR Biosciences) and band intensity was quantified with Image Studio 5.2.5 (LI-COR Biosciences).

The following primary antibodies were used for WB:

anti-AHR (rabbit, used as 1:1,000 dilution, Enzo BML-SA210),

anti-CYP1B1 (rabbit, 1:1,000, Invitrogen PA5-95277),

anti-HIF1α (rabbit, 1:500, Novus NB100-479),

anti-ATF3 (rabbit, 1:1,000, Santa Cruz sc-188),

anti-β-Actin (mouse, 1:10,000, Sigma A1978).

The following secondary antibodies and their dilutions were used for WB:

800CW donkey anti-rabbit IgG (1:10,000, LI-COR Biosciences 926-32213),

680RD donkey anti-mouse IgG (1:10,000, LI-COR Biosciences 926-68072).

Immunofluorescence

For immunofluorescence (IF) of cultured cells, cultures were washed once with PBS and then fixed in 4% ice-cold PFA for 15 min. For IF of cryosections of DRG and sciatic nerves, tissues were fixed in 4% ice-cold PFA/PBS for 12 hr, washed in PBS, soaked in 30% sucrose overnight, and then embedded in OCT compound (Fisher Scientific 23-730-571). Cryosections were cut at 12 μm thickness and placed on SuperFrost Plus slides (VWR 48311-703) and stored at -20°C before analysis. Sections were washed with PBS and incubated in blocking buffer containing 5% normal donkey serum (Jackson Immunoresearch 017-000-121) and 0.3% Triton X-100 (Acros Organics 9002-93-1) in PBS for 1 hr at room temperature. Primary antibodies were diluted in antibody dilution buffer containing 1% BSA (Fisher BioReagents BP9700100) and 0.3% Triton X-100 in PBS and incubated at 4°C overnight. Alexa-coupled secondary antibodies were diluted in antibody dilution buffer and added on sections after 3x washing with PBS and incubated for 1 hr at room temperature. DAPI (Invitrogen D1306) was used for nuclear counterstaining (1:1,000). Slides were washed 3x with PBS and mounted with Fluromount G (Southern Biotech 0100-01). Wholemount staining of footpad was performed as previously described[3]. Briefly, the footpad skin of the injured hind paw was dissected, cleaned from connective tissue, washed with PBS, and fixed in 4% PFA overnight at 4 °C. Tissue was rinsed 10x 30 min with PBS containing 0.3% Triton-X (0.3% PBST) followed by incubation with primary antibody in blocking buffer (0.3% PBST containing 5% goat serum and 20% DMSO) for 5 days at room-temperature (RT) with gentle shaking. Tissue was washed 10x 30 min with 0.3% PBST and incubated with secondary antibody in blocking buffer for 3 days at RT with gentle shaking. Subsequently, tissue was washed 10x 30 min with 0.3% PBST, dehydrated in 50% methanol for 5 min, 100% methanol for 20 min, and cleared in 1:2 ratio of benzyl alcohol: benzyl benzoate mix

overnight at RT. Imaging was performed in clearance solution with a Zeiss LSM 780 confocal microscope.

The following primary antibodies were used for IF:

anti-AHR (rabbit, 1:300, Enzo BML-SA210),

anti-ATF3 (rabbit, 1:300, Santa Cruz sc-188),

anti-Tubulin β3 (TUBB3, clone TUJ1, mouse, 1:1,000, Biolegend 801201),

anti-Tubulin β3 (TUBB3, clone TUJ1, rabbit, 1:300, Cell Signaling 5568S),

anti-SCG10/STMN2 (rabbit, 1:1,000, Novus NBP1-49461),

anti-GFP (chicken, 1:1,000, Aves Lab GFP-1020),

anti-IBA1 (rabbit, 1:1,000, Wako 019-19741),

anti-pSMAD1/5/8(rabbit, 1:1,000, Cell Signaling 9511),

anti-GAP43(rabbit, 1:1,000, Sigma AB5220),

anti-pCREB (rabbit, 1:300, Cell Signaling 9198),

anti-pS6KS235/236 (rabbit, 1:300, Cell Signaling 2211),

anti-CD45(rat, 1:50, BD Bioscience 550539),

anti-5hmC (rabbit, 1:500, Active Motif 39769).

anti-Nestin (mouse, 1:200, R&D IC1259G)

anti-Pax6 (rabbit, 1:100, Biolegend 901302).

anti-CD8a (rat, 1:100, Invitrogen 14-0081-82)

anti-CD4 (rat, 1:100, Invitrogen 14-0041-82)

anti-CD68 (rat, 1:100, Biolegend 137002)

anti-CD45 (rat, 1:100, BD Pharmingen 550539)

anti-CD11b (mouse, 1:500, ebiosciences 14-0112-82)

anti-PU1 (rabbit, 1:300, Thermofisher MA5-15064)

anti-F4/80 (rat, 1:300, Thermofisher 14-4801-81)

anti-CD206 (goat, 1:200, R&D systems AF2535)

anti-Sox10 (goat, 1:50, R&D systems AF2864)

anti-PGP9.5 (rabbit, 1:800, Neuomics, RA12103)

The following Alexa-conjugated donkey secondary antibodies (Jackson ImmunoResearch) were used at 1:300 dilution of a 1 mg/ml stock solution (in 50% glycerol).

AlexaFluor 488 anti-rabbit IgG (711-545-152),

AlexaFluor 488 anti-chicken IgY (703-545-155),

AlexaFluor 594 anti-rabbit IgG (711-585-152),

AlexaFluor 594 anti-mouse IgG (711-585-150),

AlexaFluor 594 anti-rat IgG (712-585-153),

AlexaFluor 647 anti-rabbit IgG (711-605-152),

AlexaFluor 647 anti-mouse IgG (715-605-151).

Mouse intestinal tissue preparation

Mouse intestines were prepared according to the Swiss-roll methodology that enhances epithelial morphology as described [94,95]. Briefly, mouse intestines were isolated from freshly euthanized mice and placed immediately in ice cold PBS. Intestines were carefully handled with forceps and flushed multiple times using a 20 mL syringe to clear stool and any remaining debris. At this stage, the colon and small intestines were cut and handled separately. A 1 mL glass pipette was inserted into the tissue and carefully laid on a large piece of Whatman filter paper. A sharp blade was used to cut intestines longitudinally down the length of the pipette which was then lightly rolled sideways to flatten the tissue on filter paper. The flattened tissue was subsequently rolled on a Gmark wooden swab stick and immersed in ice cold 4% PFA for overnight fixation at 4 °C. Next day, intestines were washed 3X with ice cold PBS and soaked in 15% followed by 30% sucrose/PBS solution each overnight to preserve

tissue morphology. Tissues were subsequently embedded in OCT, sectioned, and stained as described above.

Image analysis

Images of mouse DRG neuron, human induced neurons, sciatic nerve, DRG, and intestinal tissues IF images were captured using a Zeiss microscope with AxioCam MRm camera and quantification was performed as previously detailed [3]. For mouse adult cortical neuron culture, images were acquired using ImageXpress (IXM) Micro Confocal High-Content Imaging System (Molecular Devices). Unless otherwise indicated, all images were analyzed using Image J (version 2.3.0/1.53q). The length of the longest neurite of each neurite-bearing neuron (neurite longer than the diameter of its soma) was measured using the Simple Neurite Tracer (SNT version 4.0.3) plugin. The percentage of neurite bearing neurons was calculated by counting neurons with neurites longer than the diameter of soma relative to total neurons. Quantification of cytoplasmic to nuclear shuttling was performed by measuring nuclear signal relative to total signal for each individual neuron. For DRG tissue image analysis, the threshold function was used to quantify percent area per section or cell number relative to total determined by DAPI staining. Quantification of cell markers in intestines was conducted by manual cell counting in multiple villi per section.

Adult mouse cortical neuron images were quantified using the Neurite Outgrowth Analysis Module in MetaXpress 6 software (Molecular Devices). The number of valid neurons is determined by quantifying the number of $TUBB3^{+}/DAPI^{+}$ cells in a well with ≥ 10 µm of total neurite outgrowth. Total neurite outgrowth is determined by dividing the length of all neurites in a well by the number of valid neurons in that respective well.

For regeneration index, tiled images of sciatic nerves were merged using Photoshop CC 2019. The

SCG10 fluorescence intensity was measured along the length of the nerve using ImageJ. A rectangular region-of-interest (ROI) containing the lesion site, and adjacent proximal and distal areas, was selected to generate a 'plot profile'. The 'plot profile' function displays column-average gray values, with x-axis representing horizontal distance and y-axis averaged pixel intensity of columns. The position with maximal SCG10 profile intensity was used to normalize the regeneration index and the position with minimal intensity was used for subtraction of background value. Most distal SCG10 fluorescence intensity above background levels was used to determine maximal axonal length. For skin reinnervation analysis, maximal intensity projections of 400 μm z-stack was used for quantification of percentage of PGP9.5+ puncta normalized to the area of footpad using image J.

Motor and sensory behavioral testing

All behavioral tests were performed at the beginning of the mouse active phase (after 7 pm; mice were kept at 7 am – 7 pm light cycle) by an investigator blinded to the cohort identities. All animals were acclimated to the isolated procedure room for 30 min before testing. For motor function recovery testing after sciatic nerve injury, hindpaw prints were collected before and after sciatic nerve crush injury. Hindpaws were pressed on an ink pad and mice were then allowed to walk on white paper to collect the prints. The Sciatic Functional Index (SFI) was calculated by measuring dimensions of the paw prints [96], using the following formula: SFI = -38.3×(EPL-NPL)/NPL + 109.5×(ETS-NTS)/NTS + 13.3×(EIT-NIT)/NIT - 8.8 (E-, Experimental-; N-, Normal-; PL, Print Length; TS, Total Spread; IT Intermediate Toes). For sensory functional recovery, von Frey filament tests were performed [97]. The plantar surface of the hindpaw was pricked with a series of fine filaments and the mechanical threshold that evoked a withdrawal reflex was recorded. To conduct open field Basso Mouse Scale (BMS) testing, mice were placed in an open field for 5 minutes to allow 2 individuals to visually evaluate mice freely roaming to assess the following parameters: ankle movements, stepping pattern, coordination, paw placement, trunk stability, and tail movement. The mice were scored according to

the BMS scoring system [91,98,99]. Mice were tested prior to injury (baseline), 2 days post injury, and then weekly thereafter. Mice with BMS scores above 5 at 2 days post injury (incomplete injuries) or any subject that died prematurely before the end of the study was excluded from the analyses.

RNA-seq analysis

For next-generation sequencing, RNA was isolated from DRG tissue with the QIAGEN RNeasy plus mini kit sequenced on the Illumina NovaSeq platform (Psomagen). Preprocessing, quality control, and alignment of FASTQ files was performed using the NGS-Data-Charmer pipeline. Trim-Galore tool (v0.6.5) [100] was used for adaptor trimming and aligned to the mouse mm10 genome assembly using Bowtie2 (v2.4.1) [101]. The 'rmdup' module of SAMtools (v1.10) [102] was used to remove duplicated read pairs. FeatureCounts was used to obtain a gene expression matrix, using the parameters "--fraction -t gene" on the GENCODE annotation (vM25). Genes with fewer than 5 samples showing a minimum read count of 2 reads were filtered out before performing differentiation gene expression analysis with DESeq2.

Bioinformatics

TF interaction networks were generated using STRING database [26], with the default setting of medium confidence. Targeted TF binding motif analysis of RAGs was identified using Homer package [103]. ChIP-X Enrichment Analysis was performed using ChEA3 [53]. Heatmaps and volcano plots were generated with FLASKi [104] and OriginLab. Gene set enrichment analysis (GSEA) was performed using GSEA_4.3.2 software provided by the Broad Institute [105], using the non-pre ranked whole DRG genome and Hallmark_MSigDB gene sets. Pathway enrichment in gene sets was performed with IPA Qiagen knowledge database [106] and Enrichr [107,108]. IPA was also used to generate graphical summary and identify upstream regulators using default settings and with the whole list of expressed genes as

background. Identification of experimentally validated promoter motifs was conducted using the Eukaryotic Promoter Database platform [109].

Statistical analysis

For each dataset, Shapiro-Wilk test was performed to test data normality ($P > 0.05$ determined as parametric and $P < 0.05$ determined as nonparametric). For parametric data, unpaired two-tailed Student's *t*-test was used for comparison between two groups, one-way analysis of variance (ANOVA) with Holm-Sidak multiple test correction for comparison of three groups, and Two-way ANOVA followed by Benferroni's multiple comparisons test for multiple groups For nonparametric data, Mann-Whitney two-tailed *t*-test was used for comparison between two groups and Kruskal-Wallis test with Dunn's multiple test correction for comparison between multiple groups. All statistical analyses were performed with GraphPad Prism version 9 or 10. The GraphPad Prism setting NEJM (New England Journal of Medicine) for reporting of *P* values was applied. $P \leq 0.05$ was considered as statistically significant (*); $P \leq 0.01$, **; $P \leq 0.001$, ***.

Data Availability

Source data are provided with this paper. The *Ahr* cKO RNA-seq datasets are deposited at the NCBI GEO database under accession number GSE243308. <*Temporary reviewer access token is kzunkyywzzitzcd*>. The RNA-seq data of *Bmal1* cKO DRG neurons [3] has been deposited at GEO database under accession number GSE233367. The DRG 5hmC sequencing dataset [62] is available under accession code GSE85972.

Acknowledgements

We are grateful to all members from the Zou laboratory for help and suggestions. We thank Frank Gonzalez, NIH, for providing the Arnt-flox mouse line.

This work was supported by grants of the NIH (R01 NS127442), the New York State SCIRB (Spinal Cord Injury Research Board) (DOH01-C33268GG, DOH01-C30832GG, and DOH01-C32242GG), and the Neilsen Foundation (#890112) to H.Z, and by NIH R21NS131834 and R01NS128101 grants to C.G.G.. Y.W. was partly supported by a scholarship fund from Xi'an Jiaotong University.

Author contributions

Conceptualization: YW, DH, RHF, HZ; Data acquisition: YW, DH, AS, JL, HN, DH, AS, CCG; Data analysis: YW, DH, AS, CCG, RHF, HZ; Bioinformatic analysis: ME, DH, YW, AR, LS; Manuscript writing: YW, DH, RHF, HZ.

Competing Interests Statement: All authors declare no competing interests.

References

1 Bersten, D. C., Sullivan, A. E., Peet, D. J. & Whitelaw, M. L. bHLH-PAS proteins in cancer. *Nat Rev Cancer* **13**, 827-841 (2013). https://doi.org/10.1038/nrc3621

2 Mulero-Navarro, S. & Fernandez-Salguero, P. M. New Trends in Aryl Hydrocarbon Receptor Biology. *Front Cell Dev Biol* **4**, 45 (2016). https://doi.org/10.3389/fcell.2016.00045

3 Halawani, D. *et al.* Circadian clock regulator Bmal1 gates axon regeneration via Tet3 epigenetics in mouse sensory neurons. *Nat Commun* **14**, 5165 (2023). https://doi.org/10.1038/s41467-023-40816-7

4 Cho, Y. *et al.* Activating Injury-Responsive Genes with Hypoxia Enhances Axon Regeneration through Neuronal HIF-1alpha. *Neuron* **88**, 720-734 (2015). https://doi.org/10.1016/j.neuron.2015.09.050

5 Rothhammer, V. & Quintana, F. J. The aryl hydrocarbon receptor: an environmental sensor integrating immune responses in health and disease. *Nat Rev Immunol* **19**, 184-197 (2019). https://doi.org/10.1038/s41577-019-0125-8

6 Avilla, M. N., Malecki, K. M. C., Hahn, M. E., Wilson, R. H. & Bradfield, C. A. The Ah Receptor: Adaptive Metabolism, Ligand Diversity, and the Xenokine Model. *Chem Res Toxicol* **33**, 860-879 (2020). https://doi.org/10.1021/acs.chemrestox.9b00476

7 Miao, W., Hu, L., Scrivens, P. J. & Batist, G. Transcriptional regulation of NF-E2 p45-related factor (NRF2) expression by the aryl hydrocarbon receptor-xenobiotic response element signaling pathway: direct cross-talk between phase I and II drug-metabolizing enzymes. *J Biol Chem* **280**, 20340-20348 (2005). https://doi.org/10.1074/jbc.M412081200

8 Tsuji, G. *et al.* Identification of ketoconazole as an AhR-Nrf2 activator in cultured human keratinocytes: the basis of its anti-inflammatory effect. *J Invest Dermatol* **132**, 59-68 (2012). https://doi.org/10.1038/jid.2011.194

9 Schiering, C. *et al.* Feedback control of AHR signalling regulates intestinal immunity. *Nature* **542**, 242-245 (2017). https://doi.org/10.1038/nature21080

10 Vogel, C. F. A. & Haarmann-Stemmann, T. The aryl hydrocarbon receptor repressor - More than a simple feedback inhibitor of AhR signaling: Clues for its role in inflammation and cancer. *Curr Opin Toxicol* **2**, 109-119 (2017). https://doi.org/10.1016/j.cotox.2017.02.004

11 Oshima, M., Mimura, J., Yamamoto, M. & Fujii-Kuriyama, Y. Molecular mechanism of transcriptional repression of AhR repressor involving ANKRA2, HDAC4, and HDAC5. *Biochem Biophys Res Commun* **364**, 276-282 (2007). https://doi.org/10.1016/j.bbrc.2007.09.131

12 Semenza, G. L. Hypoxia-inducible factors in physiology and medicine. *Cell* **148**, 399-408 (2012). https://doi.org/10.1016/j.cell.2012.01.021

13 Vorrink, S. U. & Domann, F. E. Regulatory crosstalk and interference between the xenobiotic and hypoxia sensing pathways at the AhR-ARNT-HIF1α signaling node. *Chem Biol Interact* **218**, 82-88 (2014). https://doi.org/10.1016/j.cbi.2014.05.001

14 Gradin, K. *et al.* Functional interference between hypoxia and dioxin signal transduction pathways: competition for recruitment of the Arnt transcription factor. *Mol Cell Biol* **16**, 5221-5231 (1996). https://doi.org/10.1128/MCB.16.10.5221

15 Mandl, M. & Depping, R. Hypoxia-inducible aryl hydrocarbon receptor nuclear translocator (ARNT) (HIF-1β): is it a rare exception? *Mol Med* **20**, 215-220 (2014). https://doi.org/10.2119/molmed.2014.00032

16 Mascanfroni, I. D. *et al.* Metabolic control of type 1 regulatory T cell differentiation by AHR and HIF1-α. *Nat Med* **21**, 638-646 (2015). https://doi.org/10.1038/nm.3868

17 Gabriely, G., Wheeler, M. A., Takenaka, M. C. & Quintana, F. J. Role of AHR and HIF-1α in Glioblastoma Metabolism. *Trends Endocrinol Metab* **28**, 428-436 (2017). https://doi.org/10.1016/j.tem.2017.02.009

18 Richardson, P. M. & Issa, V. M. Peripheral injury enhances central regeneration of primary sensory neurones. *Nature* **309**, 791-793 (1984). https://doi.org/10.1038/309791a0

19 Neumann, S. & Woolf, C. J. Regeneration of dorsal column fibers into and beyond the lesion site following adult spinal cord injury. *Neuron* **23**, 83-91 (1999). https://doi.org/10.1016/s0896-6273(00)80755-2

20 Zou, H., Ho, C., Wong, K. & Tessier-Lavigne, M. Axotomy-induced Smad1 activation promotes axonal growth in adult sensory neurons. *J Neurosci* **29**, 7116-7123 (2009). https://doi.org/10.1523/JNEUROSCI.5397-08.2009

21 Seijffers, R., Mills, C. D. & Woolf, C. J. ATF3 increases the intrinsic growth state of DRG neurons to enhance peripheral nerve regeneration. *J Neurosci* **27**, 7911-7920 (2007). https://doi.org/10.1523/JNEUROSCI.5313-06.2007

22 Norsworthy, M. W. *et al.* Sox11 Expression Promotes Regeneration of Some Retinal Ganglion Cell Types but Kills Others. *Neuron* **94**, 1112-1120.e1114 (2017). https://doi.org/10.1016/j.neuron.2017.05.035

23 Ruff, C. A. *et al.* Neuronal c-Jun is required for successful axonal regeneration, but the effects of phosphorylation of its N-terminus are moderate. *J Neurochem* **121**, 607-618 (2012). https://doi.org/10.1111/j.1471-4159.2012.07706.x

24 Parikh, P. *et al.* Regeneration of axons in injured spinal cord by activation of bone morphogenetic protein/Smad1 signaling pathway in adult neurons. *Proceedings of the National Academy of Sciences* **108**, E99-E107 (2011). https://doi.org/10.1073/pnas.1100426108

25 Oñate, M. *et al.* Activation of the unfolded protein response promotes axonal regeneration after peripheral nerve injury. *Sci Rep* **6**, 21709 (2016). https://doi.org/10.1038/srep21709

26 Szklarczyk, D. *et al.* The STRING database in 2021: customizable protein-protein networks, and functional characterization of user-uploaded gene/measurement sets. *Nucleic Acids Res* **49**, D605-D612 (2021). https://doi.org/10.1093/nar/gkaa1074

27 Michaelevski, I. *et al.* Signaling to transcription networks in the neuronal retrograde injury response. *Sci Signal* **3**, ra53 (2010). https://doi.org/10.1126/scisignal.2000952

28 Song, J. *et al.* A ligand for the aryl hydrocarbon receptor isolated from lung. *Proc Natl Acad Sci U S A* **99**, 14694-14699 (2002). https://doi.org/10.1073/pnas.232562899

29 Abron, J. D. *et al.* An endogenous aryl hydrocarbon receptor ligand, ITE, induces regulatory T cells and ameliorates experimental colitis. *Am J Physiol Gastrointest Liver Physiol* **315**, G220-G230 (2018). https://doi.org/10.1152/ajpgi.00413.2017

30 Lehmann, G. M. *et al.* The aryl hydrocarbon receptor ligand ITE inhibits TGFβ1-induced human myofibroblast differentiation. *Am J Pathol* **178**, 1556-1567 (2011). https://doi.org/10.1016/j.ajpath.2010.12.025

31 Zhao, B., Degroot, D. E., Hayashi, A., He, G. & Denison, M. S. CH223191 is a ligand-selective antagonist of the Ah (Dioxin) receptor. *Toxicol Sci* **117**, 393-403 (2010). https://doi.org/10.1093/toxsci/kfq217

32 Zeisel, A. *et al.* Molecular Architecture of the Mouse Nervous System. *Cell* **174**, 999-1014.e1022 (2018). https://doi.org/10.1016/j.cell.2018.06.021

33 Sefiani, A., Rusyn, I. & Geoffroy, C. G. Novel adult cortical neuron processing and screening method illustrates sex- and age-dependent effects of pharmaceutical compounds. *Sci Rep* **12**, 13125 (2022). https://doi.org/10.1038/s41598-022-17389-4

34 Walisser, J. A., Glover, E., Pande, K., Liss, A. L. & Bradfield, C. A. Aryl hydrocarbon receptor-dependent liver development and hepatotoxicity are mediated by different cell types. *Proc Natl Acad Sci U S A* **102**, 17858-17863 (2005). https://doi.org/10.1073/pnas.0504757102

35 Giusti, S. A. *et al.* Behavioral phenotyping of Nestin-Cre mice: implications for genetic mouse models of psychiatric disorders. *J Psychiatr Res* **55**, 87-95 (2014). https://doi.org/10.1016/j.jpsychires.2014.04.002

36 Juricek, L. *et al.* AhR-deficiency as a cause of demyelinating disease and inflammation. *Sci Rep* **7**, 9794 (2017). https://doi.org/10.1038/s41598-017-09621-3

37 Shackleford, G. *et al.* Involvement of Aryl hydrocarbon receptor in myelination and in human nerve sheath tumorigenesis. *Proc Natl Acad Sci U S A* **115**, E1319-E1328 (2018). https://doi.org/10.1073/pnas.1715999115

38 Shin, J. E., Geisler, S. & DiAntonio, A. Dynamic regulation of SCG10 in regenerating axons after injury. *Exp Neurol* **252**, 1-11 (2014). https://doi.org/10.1016/j.expneurol.2013.11.007

39 Heimer-McGinn, V. & Young, P. Efficient inducible Pan-neuronal cre-mediated recombination in SLICK-H transgenic mice. *Genesis* **49**, 942-949 (2011). https://doi.org/10.1002/dvg.20777

40 Young, P. *et al.* Single-neuron labeling with inducible Cre-mediated knockout in transgenic mice. *Nat Neurosci* **11**, 721-728 (2008). https://doi.org/10.1038/nn.2118

41 Mo, A. *et al.* Epigenomic Signatures of Neuronal Diversity in the Mammalian Brain. *Neuron* **86**, 1369-1384 (2015). https://doi.org/10.1016/j.neuron.2015.05.018

42 Renthal, W. *et al.* Transcriptional Reprogramming of Distinct Peripheral Sensory Neuron Subtypes after Axonal Injury. *Neuron* **108**, 128-144 e129 (2020). https://doi.org/10.1016/j.neuron.2020.07.026

43 MacPherson, L. *et al.* Aryl hydrocarbon receptor repressor and TiPARP (ARTD14) use similar, but also distinct mechanisms to repress aryl hydrocarbon receptor signaling. *Int J Mol Sci* **15**, 7939-7957 (2014). https://doi.org/10.3390/ijms15057939

44 Cuartero, M. I. *et al.* L-kynurenine/aryl hydrocarbon receptor pathway mediates brain damage after experimental stroke. *Circulation* **130**, 2040-2051 (2014). https://doi.org/10.1161/CIRCULATIONAHA.114.011394

45 Blesch, A. *et al.* Conditioning lesions before or after spinal cord injury recruit broad genetic mechanisms that sustain axonal regeneration: superiority to camp-mediated effects. *Exp Neurol* **235**, 162-173 (2012). https://doi.org/10.1016/j.expneurol.2011.12.037

46 Hubbard, T. D., Murray, I. A. & Perdew, G. H. Indole and Tryptophan Metabolism: Endogenous and Dietary Routes to Ah Receptor Activation. *Drug Metab Dispos* **43**, 1522-1535 (2015). https://doi.org/10.1124/dmd.115.064246

47 Obata, Y. *et al.* Neuronal programming by microbiota regulates intestinal physiology. *Nature* **578**, 284-289 (2020). https://doi.org/10.1038/s41586-020-1975-8

48 Serger, E. *et al.* The gut metabolite indole-3 propionate promotes nerve regeneration and repair. *Nature* **607**, 585-592 (2022). https://doi.org/10.1038/s41586-022-04884-x

49 Huang, Z. B. *et al.* Gut microbiota-derived indole 3-propionic acid partially activates aryl hydrocarbon receptor to promote macrophage phagocytosis and attenuate septic injury. *Front Cell Infect Microbiol* **12**, 1015386 (2022). https://doi.org/10.3389/fcimb.2022.1015386

50 Sun, J. *et al.* Microbiota-derived metabolite Indoles induced aryl hydrocarbon receptor activation and inhibited neuroinflammation in APP/PS1 mice. *Brain Behav Immun* **106**, 76-88 (2022). https://doi.org/10.1016/j.bbi.2022.08.003

51 Morgan, E. W. *et al.* Contribution of Circulating Host and Microbial Tryptophan Metabolites Toward Ah Receptor Activation. *Int J Tryptophan Res* **16**, 11786469231182510 (2023). https://doi.org/10.1177/11786469231182510

52 Goto, K. *et al.* In vivo imaging of enteric neurogenesis in the deep tissue of mouse small intestine. *PLoS One* **8**, e54814 (2013). https://doi.org/10.1371/journal.pone.0054814

53 Keenan, A. B. *et al.* ChEA3: transcription factor enrichment analysis by orthogonal omics integration. *Nucleic Acids Res* **47**, W212-W224 (2019). https://doi.org/10.1093/nar/gkz446

54 Liu, Y. *et al.* Repulsive Wnt signaling inhibits axon regeneration after CNS injury. *J Neurosci* **28**, 8376-8382 (2008). https://doi.org/10.1523/JNEUROSCI.1939-08.2008

55 Zou, Y. Wnt signaling in axon guidance. *Trends Neurosci* **27**, 528-532 (2004). https://doi.org/10.1016/j.tins.2004.06.015

56 Puttagunta, R. & Di Giovanni, S. Retinoic acid signaling in axonal regeneration. *Front Mol Neurosci* **4**, 59 (2011). https://doi.org/10.3389/fnmol.2011.00059

57 Liu, C., Li, S., Liu, T., Borjigin, J. & Lin, J. D. Transcriptional coactivator PGC-1alpha integrates the mammalian clock and energy metabolism. *Nature* **447**, 477-481 (2007). https://doi.org/10.1038/nature05767

58 Liang, H. & Ward, W. F. PGC-1alpha: a key regulator of energy metabolism. *Adv Physiol Educ* **30**, 145-151 (2006). https://doi.org/10.1152/advan.00052.2006

59 LeBleu, V. S. *et al.* PGC-1α mediates mitochondrial biogenesis and oxidative phosphorylation in cancer cells to promote metastasis. *Nat Cell Biol* **16**, 992-1003, 1001-1015 (2014). https://doi.org/10.1038/ncb3039

60 Narita, T. *et al.* Identification of a novel small molecule HIF-1alpha translation inhibitor. *Clin Cancer Res* **15**, 6128-6136 (2009). https://doi.org/10.1158/1078-0432.CCR-08-3180

61 Weng, Y. L. *et al.* An Intrinsic Epigenetic Barrier for Functional Axon Regeneration. *Neuron* **94**, 337-346 e336 (2017). https://doi.org/10.1016/j.neuron.2017.03.034

62 Loh, Y. E. *et al.* Comprehensive mapping of 5-hydroxymethylcytosine epigenetic dynamics in axon regeneration. *Epigenetics* **12**, 77-92 (2017). https://doi.org/10.1080/15592294.2016.1264560

63 Sun, L. Recent advances in the development of AHR antagonists in immuno-oncology. *RSC Med Chem* **12**, 902-914 (2021). https://doi.org/10.1039/d1md00015b

64 Zhao, X. F. *et al.* The injured sciatic nerve atlas (iSNAT), insights into the cellular and molecular basis of neural tissue degeneration and regeneration. *Elife* **11** (2022). https://doi.org/10.7554/eLife.80881

65 Jager, S. E. *et al.* Comparative transcriptional analysis of satellite glial cell injury response. *Wellcome Open Res* **7**, 156 (2022). https://doi.org/10.12688/wellcomeopenres.17885.1

66 Rothhammer, V. *et al.* Aryl Hydrocarbon Receptor Activation in Astrocytes by Laquinimod Ameliorates Autoimmune Inflammation in the CNS. *Neurol Neuroimmunol Neuroinflamm* **8** (2021). https://doi.org/10.1212/NXI.0000000000000946

67 Wang, K. *et al.* Single-cell transcriptomic analysis of somatosensory neurons uncovers temporal development of neuropathic pain. *Cell Res* **31**, 904-918 (2021). https://doi.org/10.1038/s41422-021-00479-9

68 Dieci, G., Fiorino, G., Castelnuovo, M., Teichmann, M. & Pagano, A. The expanding RNA polymerase III transcriptome. *Trends Genet* **23**, 614-622 (2007). https://doi.org/10.1016/j.tig.2007.09.001

69 Costa-Mattioli, M. & Walter, P. The integrated stress response: From mechanism to disease. *Science* **368** (2020). https://doi.org/10.1126/science.aat5314

70 Harding, H. P. *et al.* Regulated translation initiation controls stress-induced gene expression in mammalian cells. *Mol Cell* **6**, 1099-1108 (2000). https://doi.org/10.1016/s1097-2765(00)00108-8

71 Huang, X., Powell-Coffman, J. A. & Jin, Y. The AHR-1 aryl hydrocarbon receptor and its co-factor the AHA-1 aryl hydrocarbon receptor nuclear translocator specify GABAergic neuron cell fate in C. elegans. *Development* **131**, 819-828 (2004). https://doi.org/10.1242/dev.00959

72 Qin, H. & Powell-Coffman, J. A. The Caenorhabditis elegans aryl hydrocarbon receptor, AHR-1, regulates neuronal development. *Dev Biol* **270**, 64-75 (2004). https://doi.org/10.1016/j.ydbio.2004.02.004

73 Crews, S. T. & Brenman, J. E. Spineless provides a little backbone for dendritic morphogenesis. *Genes Dev* **20**, 2773-2778 (2006). https://doi.org/10.1101/gad.1487706

74 de la Parra, J. *et al.* AhR Deletion Promotes Aberrant Morphogenesis and Synaptic Activity of Adult-Generated Granule Neurons and Impairs Hippocampus-Dependent Memory. *eNeuro* **5** (2018). https://doi.org/10.1523/ENEURO.0370-17.2018

75 Dever, D. P. *et al.* Aryl hydrocarbon receptor deletion in cerebellar granule neuron precursors impairs neurogenesis. *Dev Neurobiol* **76**, 533-550 (2016). https://doi.org/10.1002/dneu.22330

76 Geeven, G. *et al.* LLM3D: a log-linear modeling-based method to predict functional gene regulatory interactions from genome-wide expression data. *Nucleic Acids Res* **39**, 5313-5327 (2011). https://doi.org/10.1093/nar/gkr139

77 Hervera, A. *et al.* Reactive oxygen species regulate axonal regeneration through the release of exosomal NADPH oxidase 2 complexes into injured axons. *Nat Cell Biol* **20**, 307-319 (2018). https://doi.org/10.1038/s41556-018-0039-x

78 Palmisano, I. *et al.* Epigenomic signatures underpin the axonal regenerative ability of dorsal root ganglia sensory neurons. *Nat Neurosci* **22**, 1913-1924 (2019). https://doi.org/10.1038/s41593-019-0490-4

79 Finelli, M. J., Wong, J. K. & Zou, H. Epigenetic regulation of sensory axon regeneration after spinal cord injury. *J Neurosci* **33**, 19664-19676 (2013). https://doi.org/10.1523/JNEUROSCI.0589-13.2013

80 Wong, J. K. & Zou, H. Reshaping the chromatin landscape after spinal cord injury. *Front Biol (Beijing)* **9**, 356-366 (2014). https://doi.org/10.1007/s11515-014-1329-8

81 Ohtake, F. *et al.* Modulation of oestrogen receptor signalling by association with the activated dioxin receptor. *Nature* **423**, 545-550 (2003). https://doi.org/10.1038/nature01606

82 O'Connell, E. J., Martinez, C. A., Liang, Y. G., Cistulli, P. A. & Cook, K. M. Out of breath, out of time: interactions between HIF and circadian rhythms. *Am J Physiol Cell Physiol* **319**, C533-C540 (2020). https://doi.org/10.1152/ajpcell.00305.2020

83 Winans, B. *et al.* Linking the aryl hydrocarbon receptor with altered DNA methylation patterns and developmentally induced aberrant antiviral CD8+ T cell responses. *J Immunol* **194**, 4446-4457 (2015). https://doi.org/10.4049/jimmunol.1402044

84 Smith, K. J. *et al.* Identification of a high-affinity ligand that exhibits complete aryl hydrocarbon receptor antagonism. *J Pharmacol Exp Ther* **338**, 318-327 (2011). https://doi.org/10.1124/jpet.110.178392

85 Xiao, W., Son, J., Vorrink, S. U., Domann, F. E. & Goswami, P. C. Ligand-independent activation of aryl hydrocarbon receptor signaling in PCB3-quinone treated HaCaT human keratinocytes. *Toxicol Lett* **233**, 258-266 (2015). https://doi.org/10.1016/j.toxlet.2015.02.005

86 Chen, W. C. *et al.* Aryl hydrocarbon receptor modulates stroke-induced astrogliosis and neurogenesis in the adult mouse brain. *J Neuroinflammation* **16**, 187 (2019). https://doi.org/10.1186/s12974-019-1572-7

87 García-Lara, L., Pérez-Severiano, F., González-Esquivel, D., Elizondo, G. & Segovia, J. Absence of aryl hydrocarbon receptors increases endogenous kynurenic acid levels and protects mouse brain against excitotoxic insult and oxidative stress. *J Neurosci Res* **93**, 1423-1433 (2015). https://doi.org/10.1002/jnr.23595

88 Major, J. *et al.* Endothelial AHR activity prevents lung barrier disruption in viral infection. *Nature* (2023). https://doi.org/10.1038/s41586-023-06287-y

89 Wiggins, B. G. *et al.* Endothelial sensing of AHR ligands regulates intestinal homeostasis. *Nature* (2023). https://doi.org/10.1038/s41586-023-06508-4

90 Shah, K. *et al.* Cell-intrinsic Aryl Hydrocarbon Receptor signalling is required for the resolution of injury-induced colonic stem cells. *Nat Commun* **13**, 1827 (2022). https://doi.org/10.1038/s41467-022-29098-7

91 Ghnenis, A. B. *et al.* Evaluation of the Cardiometabolic Disorders after Spinal Cord Injury in Mice. *Biology* **11**, 495 (2022).

92 Bowles, K. R., Tcw, J., Qian, L., Jadow, B. M. & Goate, A. M. Reduced variability of neural progenitor cells and improved purity of neuronal cultures using magnetic activated cell sorting. *PLoS One* **14**, e0213374 (2019). https://doi.org/10.1371/journal.pone.0213374

93 Frey, E. *et al.* An in vitro assay to study induction of the regenerative state in sensory neurons. *Exp Neurol* **263**, 350-363 (2015). https://doi.org/10.1016/j.expneurol.2014.10.012

94 Bialkowska, A. B., Ghaleb, A. M., Nandan, M. O. & Yang, V. W. Improved Swiss-rolling Technique for Intestinal Tissue Preparation for Immunohistochemical and Immunofluorescent Analyses. *J Vis Exp* (2016). https://doi.org/10.3791/54161

95 Yoneda, M., Molinolo, A. A., Ward, J. M., Kimura, S. & Goodlad, R. A. A Simple Device to Rapidly Prepare Whole Mounts of the Mouse Intestine. *J Vis Exp*, e53042 (2015). https://doi.org/10.3791/53042

96 Marcolino, A. M. *et al.* Assessment of functional recovery of sciatic nerve in rats submitted to low-level laser therapy with different fluences. An experimental study: laser in functional recovery in rats. *J Hand Microsurg* **5**, 49-53 (2013). https://doi.org/10.1007/s12593-013-0096-0

97 Li, Y. *et al.* Macrophages facilitate peripheral nerve regeneration by organizing regeneration tracks through Plexin-B2. *Genes & development* **36**, 133-148 (2022). https://doi.org/10.1101/gad.349063.121

98 Basso, D. M. *et al.* Basso Mouse Scale for locomotion detects differences in recovery after spinal cord injury in five common mouse strains. *J Neurotrauma* **23**, 635-659 (2006). https://doi.org/10.1089/neu.2006.23.635

99 Hook, M. A. *et al.* Osteopenia in a Mouse Model of Spinal Cord Injury: Effects of Age, Sex and Motor Function. *Biology (Basel)* **11** (2022). https://doi.org/10.3390/biology11020189

100 Martin, M. Cutadapt removes adapter sequences from high-throughput sequencing reads. *EMBnet.journal* **17**, 3 (2011). https://doi.org/10.14806/ej.17.1.200

101 Langmead, B. & Salzberg, S. L. Fast gapped-read alignment with Bowtie 2. *Nat Methods* **9**, 357-359 (2012). https://doi.org/10.1038/nmeth.1923

102 Danecek, P. *et al.* Twelve years of SAMtools and BCFtools. *Gigascience* **10** (2021). https://doi.org/10.1093/gigascience/giab008

103 Heinz, S. *et al.* Simple combinations of lineage-determining transcription factors prime cis-regulatory elements required for macrophage and B cell identities. *Mol Cell* **38**, 576-589 (2010). https://doi.org/10.1016/j.molcel.2010.05.004

104 Iqbal, A. *et al.* Flaski (3.12.2). *Zenodo* (2022). https://doi.org/10.5281/zenodo.7329954

105 Subramanian, A. *et al.* Gene set enrichment analysis: a knowledge-based approach for interpreting genome-wide expression profiles. *Proc Natl Acad Sci U S A* **102**, 15545-15550 (2005). https://doi.org/10.1073/pnas.0506580102

106 Krämer, A., Green, J., Pollard, J. & Tugendreich, S. Causal analysis approaches in Ingenuity Pathway Analysis. *Bioinformatics* **30**, 523-530 (2014). https://doi.org/10.1093/bioinformatics/btt703

107 Chen, E. Y. *et al.* Enrichr: interactive and collaborative HTML5 gene list enrichment analysis tool. *BMC Bioinformatics* **14**, 128 (2013). https://doi.org/10.1186/1471-2105-14-128

108 Kuleshov, M. V. *et al.* Enrichr: a comprehensive gene set enrichment analysis web server 2016 update. *Nucleic Acids Res* **44**, W90-97 (2016). https://doi.org/10.1093/nar/gkw377

109 Dreos, R., Ambrosini, G., Périer, R. C. & Bucher, P. The Eukaryotic Promoter Database: expansion of EPDnew and new promoter analysis tools. *Nucleic Acids Res* **43**, D92-96 (2015). https://doi.org/10.1093/nar/gku1111

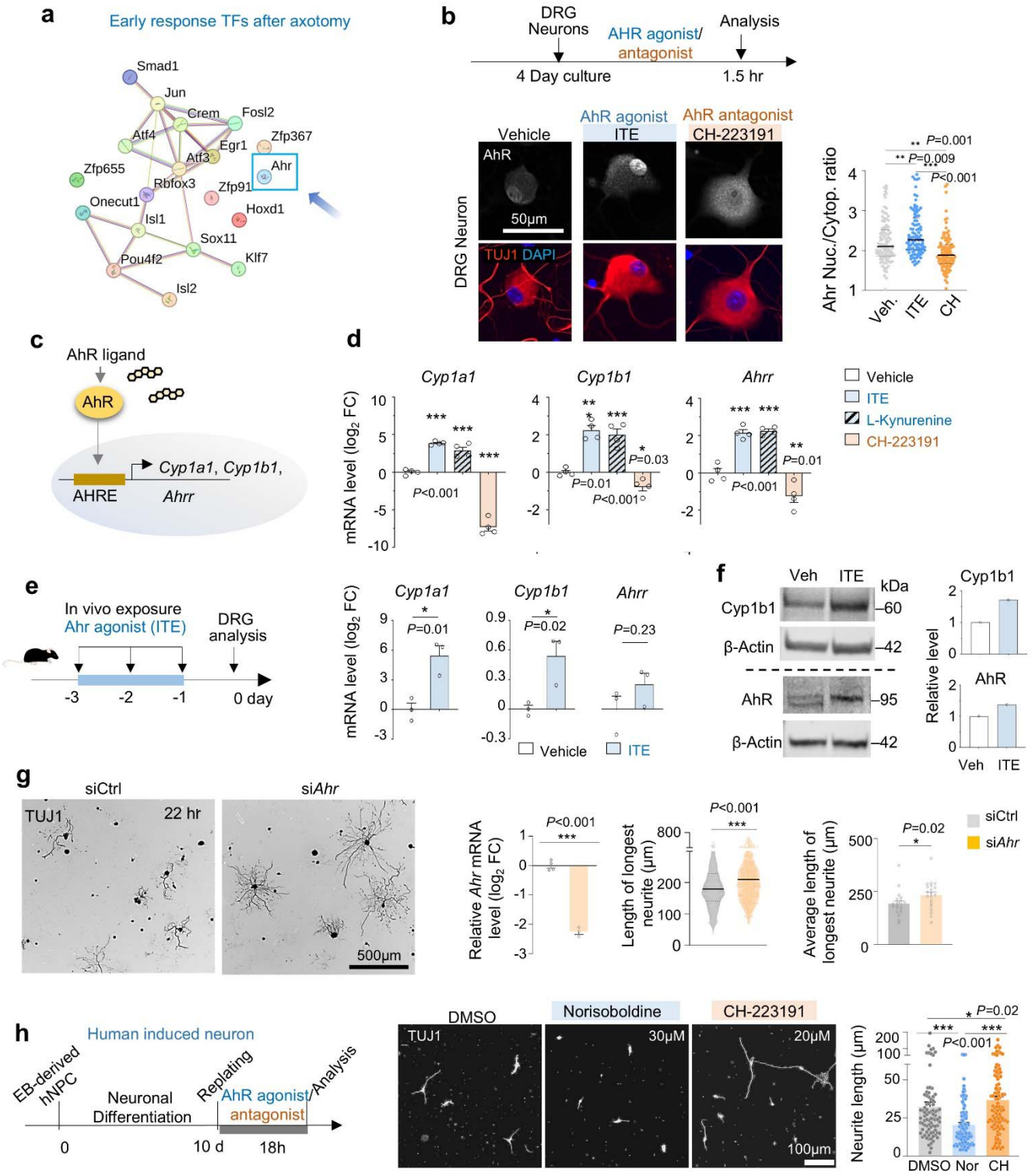

Figure 1. DRG neurons are responsive to ligand-mediated AhR signaling.

a. STRING protein-protein interaction network analysis revealed absence of known signaling link of AhR with other regeneration-associated TFs identified in our previous study (Zou et al. 2009) [1].

b. Top, schematic of primary DRG neuron cultures treated with AhR agonist, antagonist or vehicle and

analyzed 1.5 hr later. Bottom, representative IF images show changes of cytoplasm-nuclear shuttling of AhR in response to AhR agonist (ITE, 10 μM) or AhR antagonist (CH, 10 μM). Violin plots of AhR nuclear to cytoplasmic ratio for n=100 DRG neuron per condition. Black line represents median. One-way ANOVA with Dunnett's multiple test correction.

c. Diagram of ligand-mediated AhR activation to induce canonical target genes through AHR response element (AHRE).

d. qRT-PCR results of AhR target genes normalized to housekeeping gene *Hprt1* in primary DRG neurons with different drug treatments (25 μM) for 24 hr. n=4 independent DRG neuron cultures per group. Data represent mean ± SEM. One-way ANOVA with Dunnett's multiple test correction.

e. Left, experimental paradigm of adult mice receiving AhR agonist ITE (10 mg/kg; i.p, 3 daily injections) or vehicle (DMSO), followed by DRG analysis 1 day later. Right, qRT-PCR results of gene expression of AhR canonical target genes normalized to *Hprt1* in DRG from vehicle- or ITE-treated mice. n=3 independent L4-6 DRG samples from 3 mice. Data represent mean ± SEM. Unpaired two-tailed Student's *t*-test.

f. Western blots and quantifications of Cyp1b1 and AhR in DRG from vehicle- or ITE-treated mice. Note the electrophoretic mobility shift of AhR in DRGs from ITE-treated mice.

g. Left, IF images of siRNA treated DRG neurons show enhanced neurite outgrowth with *Ahr* knockdown, confirmed by qRT-PCR analysis. n=4 independent cultures for siCtrl and n=3 for si*Ahr*. Bar graphs represent mean ± SEM. Quantification of longest neurite length from n=489 neurons for siCtrl and n=482 for siAhr, pooled from 4 independent cultures for each condition. Black horizontal lines in violin plots indicated median. Mann-Whitney two-tailed test. Quantification of average longest neurite length of 25 neurons from n=20 images collected from n=4 independent cultures for each condition. Mann-Whitney two-tailed test.

h. Left, experimental schematic of AhR agonist or antagonist stimulation of human induced neurons from hESC via neuronal differentiation of embryoid body (EB) and human neuroprogenitor cells. Middle, IF images for TUJ1 of induced neurons after replating. Right, quantifications of neurite length. n=83 cells for DMSO, n=90 for NOR, n=106 for CH treatment. Data represent mean ± SEM. One-way ANOVA with Dunnett's multiple test correction.

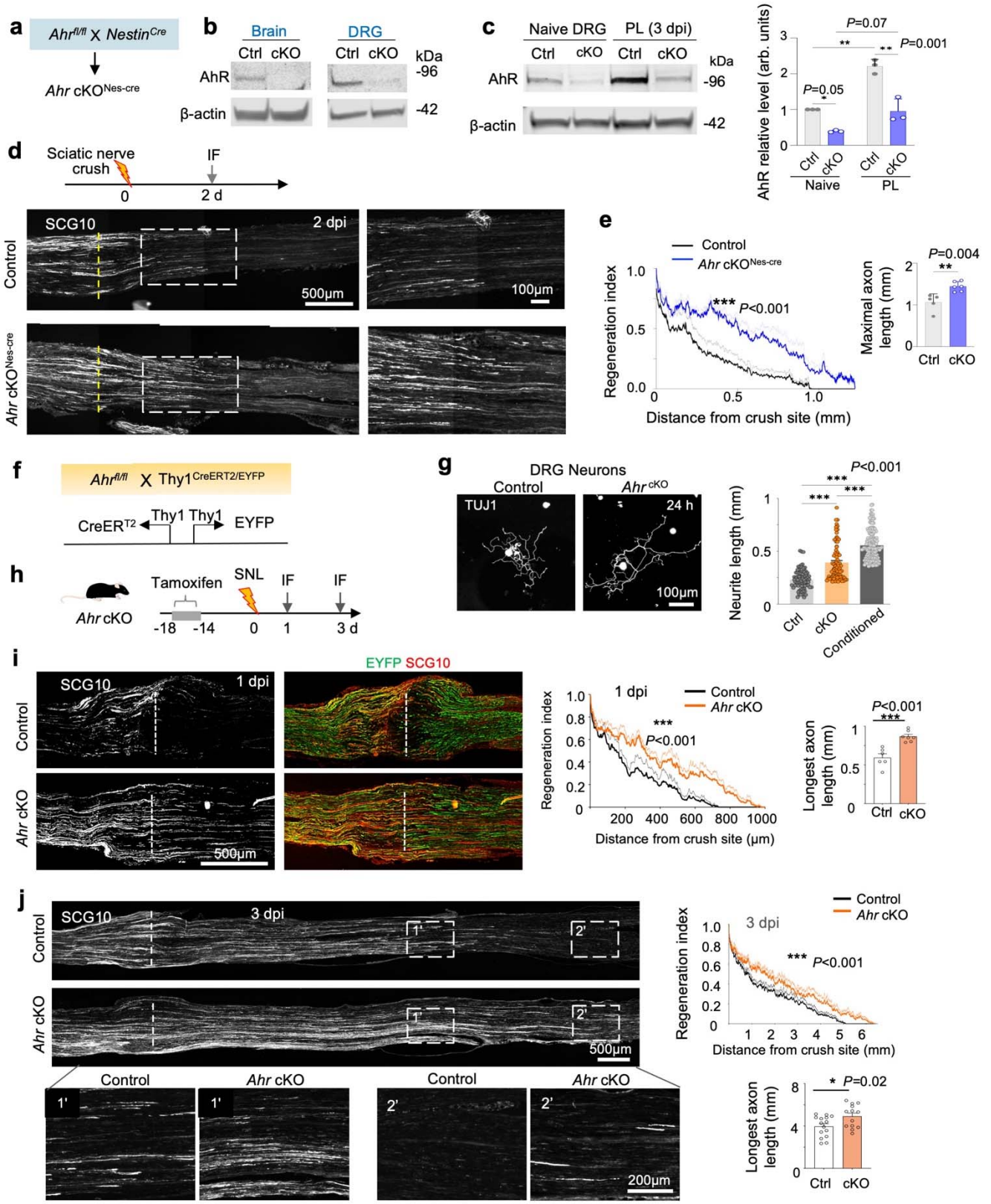

Figure 2. Neuronal AhR deletion enhances axon regeneration after sciatic nerve injury.

a. Diagram of generating *Ahr* cKO$^{Nes\text{-}cre}$ mice by breeding *Ahr* floxed mice with Nestin-Cre allele.

b. Western blots show depletion of AhR in brain and DRGs from *Ahr* cKO$^{Nes\text{-}cre}$ mice. β-actin served as loading control.

c. Western blots and quantifications show expression of AhR in naive and conditioned DRG (3 dpi after PL) from *Ahr* cKO$^{Nes\text{-}cre}$ relative to control (Ctrl) mice, β-actin as loading control. n=3 independent samples from 3 mice, each from pooled L4-L6 DRGs. Data represent mean ± SEM. Two-way ANOVA with Bonferroni multiple test correction.

d. Top, experimental paradigm. Bottom, IF images show enhanced axon regrowth (SCG10^{+}) in *Ahr* cKO$^{Nes\text{-}cre}$ mice compared to littermate controls at 2 dpi. Dashed lines denote crush center (based on highest immunointensity of SCG10).

e. Left, quantification of SCG10^{+} axons transversing lesion center. Mean + SEM. Right, bar graph of longest axon length distal to lesion center. n=5 mice for control and n=6 for cKO mice. Two-way ANOVA for regeneration index. Unpaired two-tailed Student's *t*-test for maximal axon length. Data represent mean ± SEM.

f. Diagram of crossing *Ahr*$^{fl/fl}$ allele to Thy1$^{CreERT2/EYFP}$ transgenic line expressing tamoxifen inducible CreERT2 and EYFP (driven by bidirectional Thy1 promoter).

g. IF images and quantification of neurite outgrowth (TUJ1^{+}) of primary DRG neurons from *Ahr*$^{fl/fl}$ Thy1$^{CreERT2/EYFP}$ (*Ahr* cKO) or littermate controls after tamoxifen injection (100 mg/kg; i.p., 5 consecutive days) 14 days prior. n=81, 81, and 149 for control, *Ahr* cKO, or pre-conditioned DRG neurons, respectively, collected from n=2 mice per genotype. Bar graphs represent mean ± SEM. One-way ANOVA with Dunn's multiple comparisons test. Pre-conditioned neuron dataset used from [2].

h. Experimental paradigm: tamoxifen (100 mg/kg; i.p., 5 consecutive days) administered 14 days prior to sciatic nerve crush lesion (SNL), axon regeneration assessed by IF for SCG10 at 1 and 3 dpi.

i, j. IF images and quantifications of SCG10^{+} axons traversing lesion center of crushed sciatic nerve (dashed lines) at 1 or 3 dpi. Mean + SEM. Magnified images are shown below. n=6 control and n=7 cKO mice per group for 1 dpi. n=15 control and n=13 cKO for 3 dpi. For regeneration index, two-way ANOVA with Bonferroni multiple test correction; for longest axon length distal to lesion center, unpaired two-tailed Student's *t*-test. Data represent mean ± SEM.

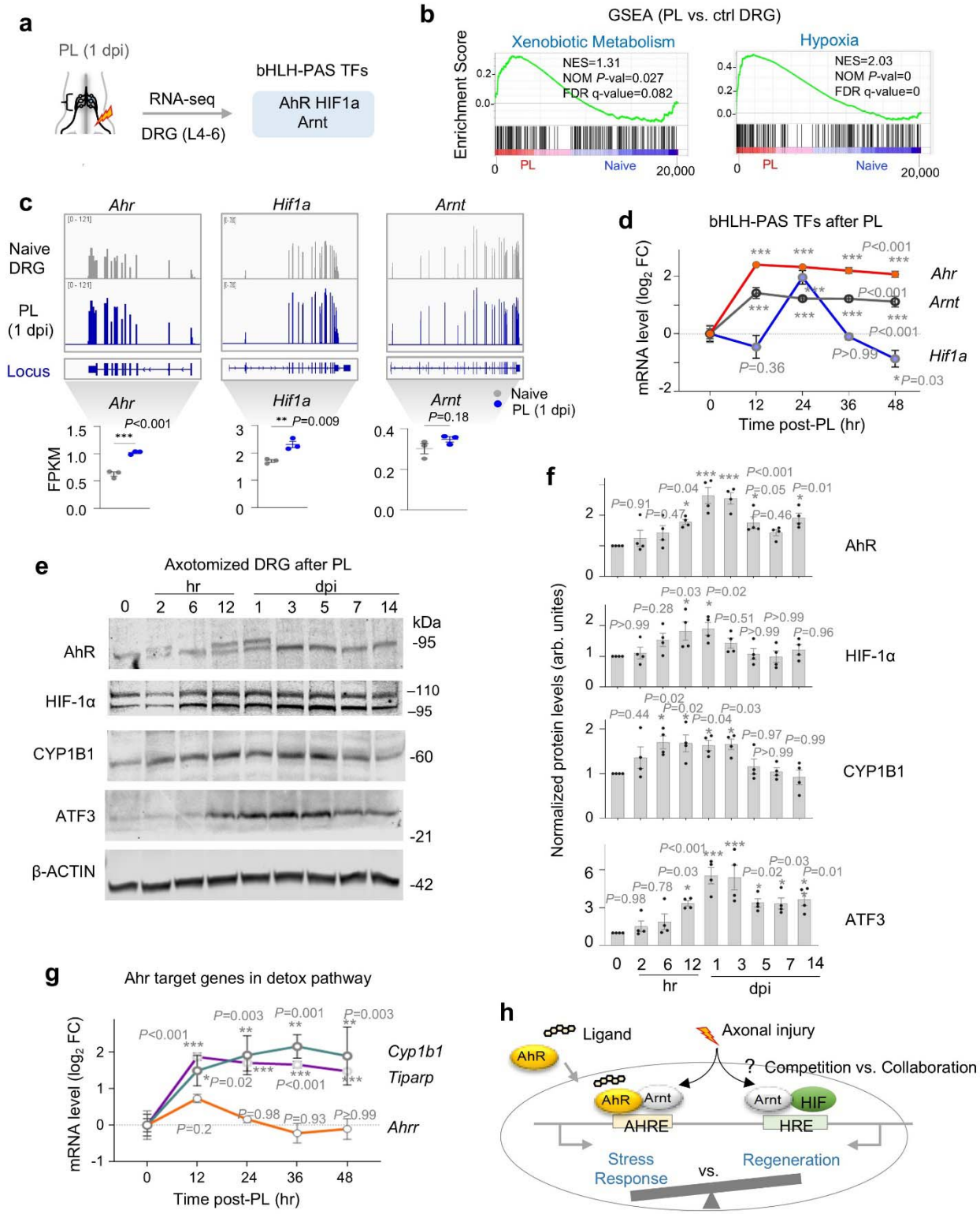

Figure 3. Peripheral lesion of DRG results in early induction of AhR and HIF-1α.

a. Diagram of RNA-seq analysis of lumbar 4-6 DRGs at 1 day after PL as compared to uninjured (naive) DRGs. bHLH-TFs are denoted in blue.

b. GSEA shows enrichment of Xenobiotic metabolism and Hypoxia in axotomized DRG at 1 dpi as

compared to naive DRG (~20,000 genes). NES, normalized enrichment score; FDR, false discovery rate.

c. Top, RNA-seq read tracks of the indicated TFs. Bottom, graphs showing FPKM (fragments per kilobase of transcript per million reads) of the genes. n=3 independent DRG samples per condition. Unpaired two-tailed Student's *t*-test.

d. Time-course qRT-PCR analyses at early time points after PL, normalized to housekeeping gene *Hprt1*. Data represent mean ± SEM. n=3 independent samples, each pooled from L4-L6 DRGs from n=3 mice per group. One-way ANOVA with Dunnett's multiple test correction. ***$P<0.001$.

e, f. Western blots (e) and quantifications (f) of protein expression in DRG at different time points after PL relative to no injury (β-actin as loading control). n=4 independent DRG samples from 4 mice per time point. Bar graphs represent mean ± SEM. One-way ANOVA with Dunnett's multiple test correction.

g. Time course qRT-PCR analyses of canonical AhR target genes in DRG after PL relative to no injury (normalized to *Hprt1*). Data represent mean ± SEM. n=3 independent samples from 3 mice per group, each pooled from L4-L6 DRGs. One-way ANOVA with Dunnett's multiple test correction.

h. Schematic model of competitive vs. collaborative interaction between AhR and HIF pathways to regulate shared or distinct injury response or regeneration-associated genes.

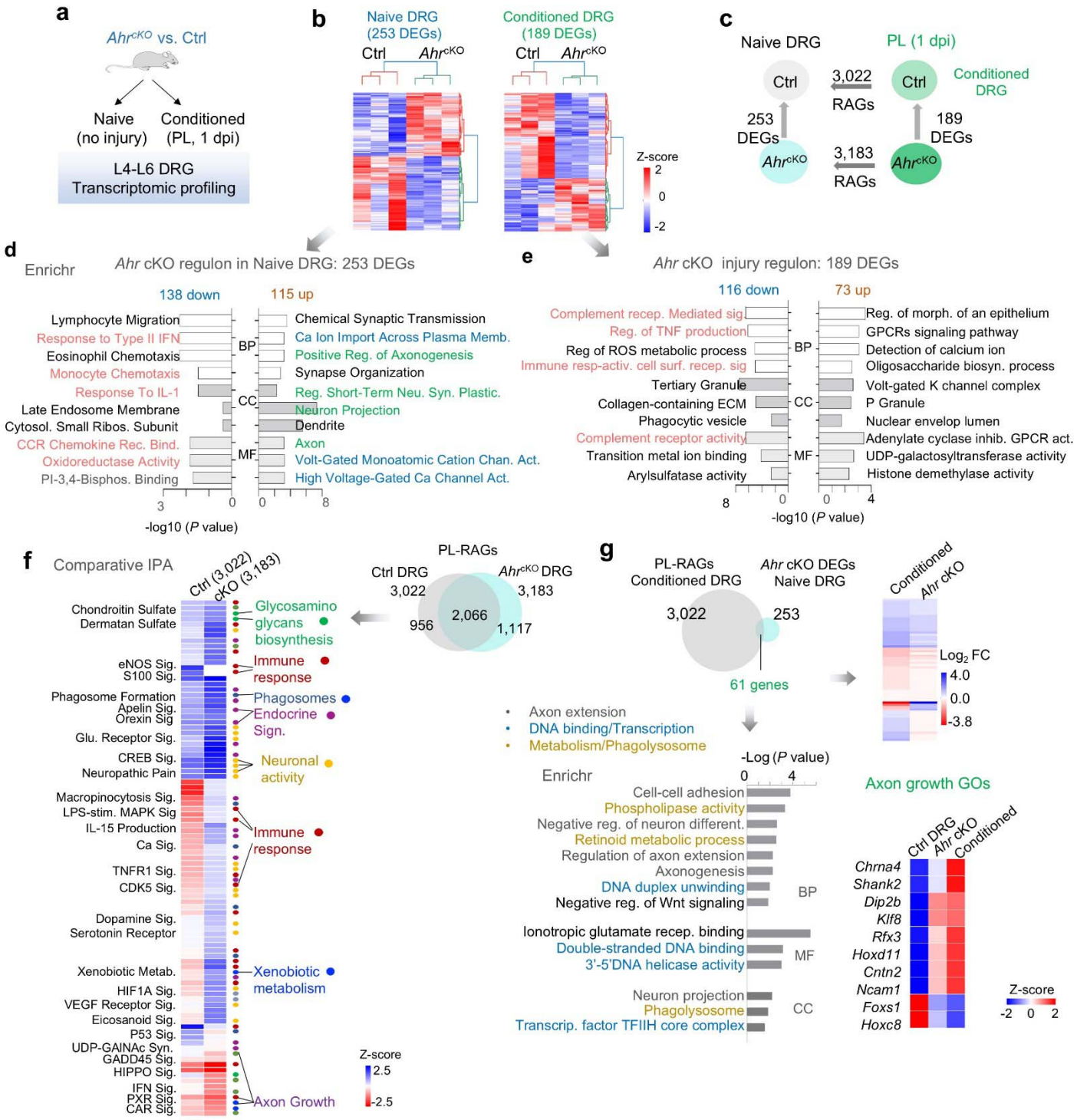

Figure 4. AhR cKO partially mimics conditioning lesion in initiating axonogenesis gene program while suppressing stress response.

a. Experimental paradigm of RNA-seq of DRG from *Ahr*^{cKO} vs. littermate controls (n=3) in naive state or after PL at 1 dpi.

b. Heatmaps of hierarchically clustered differentially expressed genes (DEGs) in *Ahr*^{cKO} vs. control

DRG in naive or axotomized state (triplicates each, cutoff: abs ($\log_2$ FC) >0.25, P <0.05).

c. Summary diagram of 4-way comparison of DEGs in control or *Ahr*^{cKO} DRGs in naive or axotomized state. PL-RAGs in control DRG (n=3,022) were previously reported (Halawani et al. 2023) [2].

d, e. Enrichr pathway analysis of up- and downregulated DEGs (*Ahr* cKO/Ctrl) in naive or axotomized DRG at 1 dpi. BP, biological process; CC, cellular component; MF, molecular function.

f. Left, comparative IPA of PL-induced regeneration associated genes (RAGs) at 1 dpi in control (n=3,022) and *Ahr*^{cKO} DRGs (n=3,183) with selected annotation on left. Colored dots on right denote pathway classification. Right, Venn diagram showing overlap of DEGs.

g. Top left, Venn diagram showing overlap of genes between PL-RAGs after conditioning lesion at 1 dpi and AhR regulon in naive DRG. Bottom left, top enriched ontologies of 61 overlapping genes. Top right, heatmap of relative expression of 61 overlapping genes. Bottom right, heatmap of relative expression of selected genes of the gene ontologies (GOs) Neuro-projection, Axonogenesis, and Axon guidance (part of the 61 overlapping RAGs).

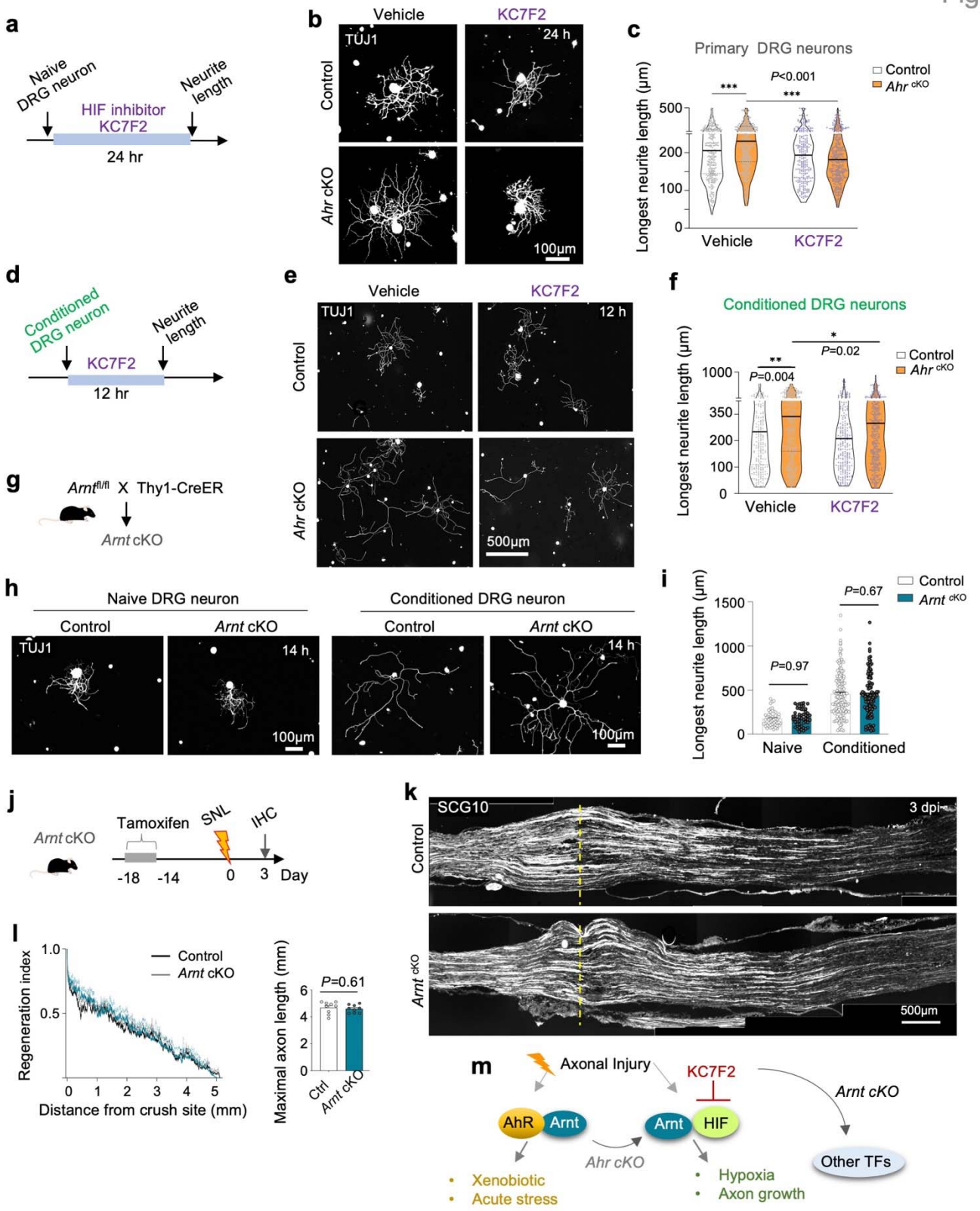

Figure 5. Growth promoting effect of *Ahr* deletion requires HIF1α.

a-f. Neurite outgrowth assay of primary DRG neurons (a-c) or conditioned DRG neurons with peripheral axotomy 3 days prior (d-f). Left, experimental schemes: DRG neurons treated with HIF1α

inhibitor KC7F2 (10 μM) and examined 24 or 12 hrs after plating. Right, representative IF images for TUJ1 and quantifications of neurite outgrowth. Violin plots of n=250-408 neurons for each condition. Horizontal black line denotes median. Two-way ANOVA followed by Bonferroni's multiple comparison test.

g. Experimental scheme for generation of *Arnt* cKO (*Arnt*$^{fl/fl}$ Thy1-CreERT2/EYFP) mice.

h, i. Representative IF images for TUJ1 and quantifications of naive or conditioned DRG neurons from *Arnt* cKO or control mice at 14 hr post-seeding. n=51-52 neurons for naive and n=122-157 for conditioned DRG neurons from n=5 mice per genotype. Bar graphs represent mean ± SEM. Two-way ANOVA followed by Bonferroni's multiple comparison test.

j-l. Experimental paradigm: sciatic nerve crush lesion (SNL) performed 14 days after tamoxifen injection (100 mg/kg; 5 daily i.p.,) and axon regrowth analyzed at 3 dpi. Representative IF images and quantification of axon regeneration (SCG10^{+}) at 3 dpi. Dashed lines: lesion center. n=9 mice per genotype. Two-way ANOVA for regeneration index. Unpaired two-tailed Student's *t* test for maximal axon length.

m. Working model of AhR and HIF competition for heterodimerization partner Arnt.

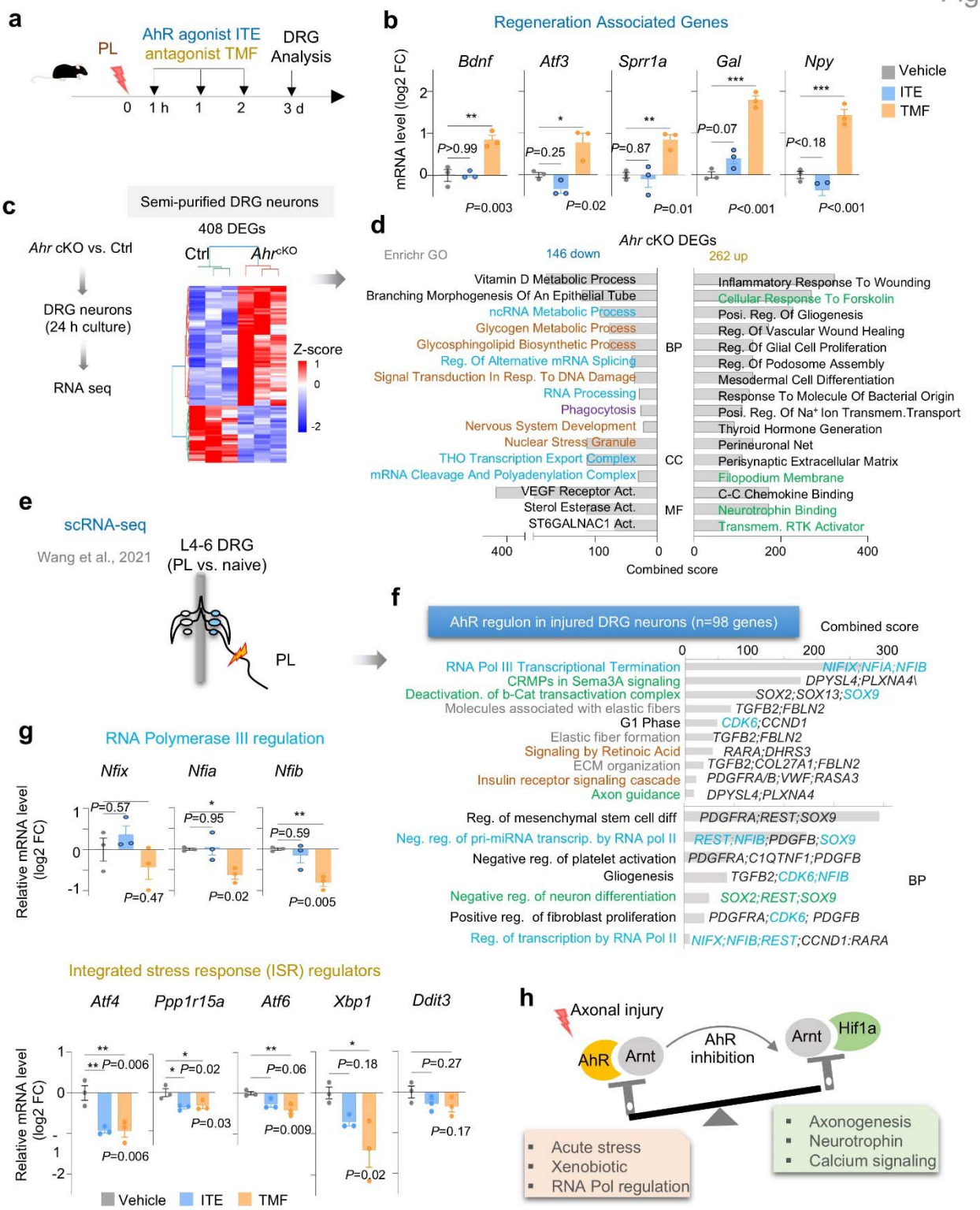

Figure 6. Pharmacological attenuation of AhR activation impacts RNA Polymerase III regulation and ISR in injured DRG.

a. Experimental paradigm of in vivo injection of AhR agonist, antagonist (10 mg/kg; i.p.) or vehicle (DMSO) after sciatic nerve crush injury. DRGs were collected for analysis at 3 dpi.

b. qRT-PCR results normalized to housekeeping gene *Hprt1* demonstrate augmented induction of RAGs with AhR antagonist TMF after PL. Data represent mean ± SEM. n=3 independent samples, each pooled from L4-L6 DRGs from 3 mice per group. One-way ANOVA with Dunnett's multiple test correction.

c. Left, experimental paradigm for semi-purified DRG neuron isolation from *Ahr* cKO or control mice for RNA-seq analysis at 24 hr post-seeding. Right, heatmap of the DEGs (*Ahr* ^{cKO} vs. Ctrl) from triplicate samples of semi-purified DRG neurons isolated from n=3 mice per group, cutoff: abs ($\log_2$ FC) >0.25, P <0.01.

d. Enrichr analysis reveals top pathways for the 408 DEGs (*Ahr* cKO vs. control) in semi-purified DRG neurons (axotomized during dissociation). BP, biological process; CC, cellular component; MF, molecular function.

e. Schematic of scRNA-seq of axotomized DRG after sciatic nerve injury relative to no injury DRG (Wang et al. 2021) [3]. Predicted AhR regulon of 98 genes based on bioinformatic analysis of TFs driving DEGs across a time-course of 6, 24 hr, 2, 7, and 14 days in DRG neurons after axotomy.

f. Enrichr analysis reveals top pathways for the 98 predicted DRG neuron specific AhR regulon genes after PL from scRNA-seq. BP, biological process.

g. qRT-PCR analysis of genes from the indicated Enrichr GO terms shown above. Results were normalized to housekeeping gene *Hprt1*. Data represent mean ± SEM. n=3 independent samples, each pooled from L4-L6 DRGs from 3 mice per group. One-way ANOVA with Dunnett's multiple test correction.

h. Working model of the role of AhR in balancing neural injury and regenerative responses.

References in Figure Legends

1 Zou, H., Ho, C., Wong, K. & Tessier-Lavigne, M. Axotomy-induced Smad1 activation promotes axonal growth in adult sensory neurons. *J Neurosci* **29**, 7116-7123 (2009). https://doi.org/10.1523/jneurosci.5397-08.2009

2 Halawani, D. *et al.* Circadian clock regulator Bmal1 gates axon regeneration via Tet3 epigenetics in mouse sensory neurons. *Nat Commun* **14**, 5165 (2023). https://doi.org/10.1038/s41467-023-40816-7

3 Wang, K. *et al.* Single-cell transcriptomic analysis of somatosensory neurons uncovers temporal development of neuropathic pain. *Cell Res* **31**, 904-918 (2021). https://doi.org/10.1038/s41422-021-00479-9